# Effects of FACTS devices on Static Voltage Collapse Phenomena

by

Zeno T. Faur

A thesis
presented to the University of Waterloo
in fulfillment of the
thesis requirement for the degree of
Master of Applied Science
in
Electrical Engineering

Waterloo, Ontario, Canada, 1996

I hereby declare that I am the sole author of this thesis.

I authorize the University of Waterloo to lend this thesis to other institutions or individuals for the purpose of scholarly research.

I further authorize the University of Waterloo to reproduce this thesis by photocopying or by other means, in total or in part, at the request of other institutions or individuals for the purpose of scholarly research.

The University of Waterloo requires the signatures of all persons using or photocopying this thesis. Please sign below, and give address and date.

# Abstract

This thesis presents the steady-state modelling of some Flexible Alternative Current Transmission Systems (FACTS) devices, namely, Static Var Compensators (SVC) and Thyristor Controlled Series Capacitors (TCSC), with their controls and limits. The proposed steady-state models are validated by dynamical simulation of the equivalent circuit. Handling of limits, control mode switching, and their implementation in the power flow are presented and discussed.

Bifurcation analysis is applied in order to find the optimal location and rating of these devices and a continuation power flow is used to evaluate the effects of FACTS on the system loadability for several power systems. Eigenvector analysis applied at the maximum loading point is used to locate and design the FACTS devices such that the distance to this point is maximized.

The models and the methodology for placing and designing FACTS are tested in a 12 bus ac system and a 173 bus ac/dc system. The results are presented and discussed. Performance factors to evaluate the impact of FACTS devices on the operation of a power system are proposed and used to assess the efficiency of FACTS devices.

# Acknowledgements

The author would like to thank Professor Claudio A. Canizares for the opportunity to do this research, and for his guidance and support.

Thanks are also due to my colleagues for many helpful and interesting discussions.

The support and encouragement of my family and friends has been invaluable and is greatly appreciated.

*" ... If you can dream - and not make dreams your master;*

*If you can think - and not make thoughts your aim, ...*

*... If all men count with you, but none too much;*

*If you can fill the unforgiving minute*

*With sixty seconds' worth of distance run,*

*Yours is the Earth and everything that's in it,*

*And - which is more - you'll be a Man, my son ! "*

( From the poem *"If"* by Rudyard Kipling )

I wish to dedicate this thesis to my parents, Lidia and Teofil Faur. They offered me their love and wisdom, without them I would not be the person I am.

# Contents

# List of Figures

# List of Tables

# Principal symbols

**FACTS** Flexible Alternative Current Transmission Systems

**TCSC** Thyristor Controlled Series Capacitor

**SVC** Static Var Compensator

**STATCOM** Static Compensator

**UPFC** Universal Power Flow Controller

**HVDC** High Voltage Direct Current link

**TCR** Thyristor Controlled Reactor

**FC-TCR** Fixed Capacitor-Thyristor Controlled Reactor

**TSC-TCR** Thyristor Switched Capacitor-Thyristor Controlled Reactor

**MOV** Metal Oxide Varistor

$\delta_t$ Transmission angle (angular difference between line end voltages)

$X_L$ 60 Hz inductor reactance

$X_C$ 60 Hz capacitor reactance

$X_V$ variable reactance

$B_V$ variable susceptance

$X_e$ equivalent reactance

$B_e$ equivalent susceptance

# Chapter 1

# Introduction

## 1.1 Voltage Collapse

Alternative current power systems typically tend to be operated below the surge impedance load of their transmission lines and considerably under the thermal ratings of the lines. Increasing economic, legal and environmental pressures have forced utilities to operate their power networks closer to their margin of steady-state stability. The increased use of existing transmission is made possible, in part, by reactive power compensation which is inherently less robust than "wire-in-the-air". Power transmission capability has traditionally been limited by either rotor angle (synchronous) stability or by thermal loading capabilities [1]. More recently, voltage instability has been considered as another limiting factor to power transmission. Over the last ten to fifteen years, the electric power industry has become increasingly concerned with voltage instability and collapse. This concern is based on several voltage collapse incidents as described in an IEEE report [2].

As some parameters in the system change, in particular the system load, the voltage magnitudes slowly decline. System operators usually control the voltages at some buses by increasing reactive generation, capacitor switching and/or tap changing. As some devices reach their limits, the ability of controling the voltages is lost; furthermore, at a certain loading of the system one type of instability that may occur is voltage collapse. This phenomenon is characterized by a sharp and fast decrease in voltage magnitude at some or all buses. This is now a major concern in planning and operation of electric power systems.

The main factor causing voltage collapse is the inability of the power system to meet the demand for power [3]. A power system at a given operating state and subject to a given disturbance undergoes *voltage collapse* if it is voltage unstable or if the post-disturbance equilibrium values are below acceptable limits. The acceptable limits are system and load dependent. Voltage collapse may be total (blackout) or partial [3].

While voltage collapse can be associated with loss of synchronism for generators, the phenomenon can also occur where rotor angle stability is not an issue. Different mechanisms have been identified for voltage collapse. If reactive power control is lost at the source due to manual control or field current limiters of the synchronous machines, voltage collapse at the load may follow [3].

Voltage collapse can also occur in the case of increased stress on a load area where voltage support is inadequate. Tap changers reaching limits and large induction motor loads are factors which play an important role in voltage instability [3].

Another example of voltage instability is the case of an HVDC inverter operating at fixed extinction angle and supplying constant power to a weak ac system. Voltage instability can occur during the recovery of the DC power following a severe disturbance or when the DC power is increased beyond its critical level [3].

In the past few years, a great deal of attention has been given to develop various methods for studying voltage stability. They range from the very simple to the highly complex and can be classified mainly into static and dynamic approaches [5].

Voltage instability and collapse dynamics span a range in time from a fraction of a second to tens of minutes. The phenomena associated with voltage dynamics have been classified into transient and longer-term voltage stability. The time frame for transient voltage stability is up to about ten seconds. Rotor angle instability and voltage instability are associated, and aspects of both phenomena may exist. Transient stability studies are performed to investigate this type of problem with dynamical models of the system.

Longer-term voltage instability phenomena span over a time frame of minutes to hours. This scenario involves high loads, generators, tap changers and other devices hitting limits and eventually partial or complete voltage collapse [1].

Static voltage collapse phenomena are associated with loss of steady-state stability for a power system. Steady-state stability refers to the dynamic system response to small disturbances that continuously occur during the operation of a system. This

problem can be studied by looking at the linearized dynamic equations of the system at an operating point. Thus, a power system is steady-state stable for a particular operating condition if, following any small disturbance, the system reaches a steady-state condition [4]. The stability condition is determined by calculating the eigenvalues of the linearized system; if all real parts of the eigenvalues are negative, the system is stable; otherwise, it is unstable.

From the many existing static techniques the continuation power flow is used in this thesis [6]. This is a step-by-step or "snapshot" method that analyzes the solutions of the power flow as a parameter in the system, namely the load, is discretely increased. Adequate models for all devices including controls and limits are crucial in order to obtain good results. Also, specific knowledge of the system, i.e., structure and distribution of loads, is required in order to buildup a credible scenario. This approach is computationally less intensive and provides significant insight into some of the instability mechanisms, thus making it attractive for the study of large systems.

Today, virtually all power system transmission and generation planning, as well as operating, is performed using assumed load distributions and growth rates based on load forecasts; therefore, a stability margin obtained using load forecast information may be in fact the most practical measure available to planners and operators [7].

## 1.2 FACTS devices

Todays power systems are large and widely interconnected, probably the most complex man-built systems. The purpose of the transmission network is to pool power plants and load centers in order to supply the load at a required reliability and maximum efficiency at a lower cost. In North-America, inter-regional power transfers have been growing much faster than transmission capacity.

As power transfers grow, the power system can become increasingly more difficult to operate, and the system becomes more insecure with unscheduled power flows and higher losses. In this context, the Electric Power Research Institute (EPRI) has put forward a concept called Flexible Alternative Current Transmission System (FACTS). The objective of FACTS technology is to bring a system under control and to transmit power as ordered by the control centre; it also allows to increase the usable transmission capacity to its maximum thermal limits [8].

Power systems of today by and large are mechanically controlled. With mechan-

ical devices, such as circuit breakers, control cannot be initiated frequently because mechanical devices tend to wear out quickly compared to static devices. The central technology of FACTS involves high power electronics, a variety of thyristor devices, microelectronics, communications and advanced control centers [8].

Power flow through an ac line is a function of phase angle, line end voltages and line impedance, and there is little or no control over any of these variables. The consequences of this lack of fast, reliable control are stability problems, power flowing through other than the intended lines, the inability to fully utilize the transmission resources, undesirable var flows, higher losses, high or low voltages, cascade tripping and long restoration times. With FACTS devices one can control the phase angle, the voltage magnitude at chosen buses and/or line impedances. Power flow is electronically controlled and it flows as ordered by the control center [8].

The range of FACTS devices include:

- Static Var Compensators (SVC)
- Static Compensators (STATCOM)
- Thyristor Controlled Series Capacitors (TCSC)
- Universal Power Flow Controllers (UPFC)
- High Voltage Direct Current Transmission (HVDC)

From these, this thesis will concentrate on the SVC and the TCSC, both of which are currently applied.

## 1.3 Thesis outline

Chapter 1 introduces the reader to the voltage collapse phenomena and to FACTS devices. Chapter 2 presents aspects of bifurcation theory as they relate to voltage collapse phenomena. In Chapter 3, steady-state models of an SVC and a TCSC are derived and compared to dynamical models, then different control strategies are discussed for each of these devices.

A methodology to implement these FACTS devices in a power flow is presented in Chapter 4 together with the continuation power flow, which is the chosen technique,

in this thesis, to investigate voltage instability in a power system. Chapter 5 presents a method of locating and designing these devices based on the bifurcation analysis of a 12 bus ac system . The results of the studies performed on a 173 bus ac/dc system are presented in Chapter 6, and a performance measure is proposed to assess the effect of FACTS devices on the system. Chapter 7 presents the conclusions of this thesis.

# Chapter 2

# Saddle-node bifurcations

## 2.1 Saddle-node bifurcations in AC/DC power systems

Nonlinear phenomena such as jumping between modes, vanishing of periodic oscillations, loss or gain of stability and chaos, arise in all fields of physics, chemistry, biology and engineering. The classical mathematical discipline that treats this kind of nonlinear phenomena is bifurcation theory [9].

In [10] the authors suggest that static voltage collapse may be explained as a dynamic consequence of a generic saddle-node bifurcation. At this bifurcation, the system state leaves the bifurcating equilibrium point and moves along a particular trajectory. The authors consider a nonlinear dynamical power system model described by a system of ordinary differential equations (ODE) of the type :

$$\dot{\mathbf{x}} = \mathbf{f}(\mathbf{x}) \tag{2.1}$$

where a singular perturbation technique is used to obtain this model from the typical differential-algebraic model of the power system, based on the idea that algebraic equations are presumably idealizations of some unmodelled dynamics.

In [11] the authors use center manifold theory to study how the voltage collapse problem occurs in power sytems. Saddle-node bifurcations are typically associated

with dynamical models represented by differential equations [9, 11]; however, power system models represented by differential equations with algebraic constraints (DAE) have been shown to exhibit the same type of bifurcations [12].

The main condition for the bifurcation point in *certain* differential and differential-algebraic models is the singularity of the power flow Jacobian, which is associated with the voltage collapse phenomena in [7, 12, 13, 14]. The power flow equations are actually a subset of the full steady-state equations [12].

Dynamic events such as large disturbances may drive the system to instability without any bifurcation occurring in the system. In a bifurcation related voltage collapse, the parameters in the system are changing quasi-statically. For these reasons, voltage stability problems related to bifurcations have been labeled as "static" voltage phenomena. It should be mentioned here that not all static voltage collapse problems are caused by saddle-node bifurcations (e.g. [15, 16]).

In this thesis, voltage collapse phenomena are associated with saddle-node bifurcations of the dynamical model of the power system, and the equivalency conditions [12, 13, 16] are used to detect the bifurcation point.

The scenario that is typically considered is that the load is discretely increased and a series of load flows are solved, providing snapshots of the system trajectory. The device limits and controls play an important role here. The snapshot approach is a compromise between a detailed time domain simulation and a static approach. This quasi-dynamic approach provides comprehensive information regarding the mechanism of instability with lower CPU requirements. The snapshots will approximate the time domain trajectory, disregarding the small oscillations due to the incremental changes in load. However, with proper models of the power system components, including their controls and limits, the technique is able to determine if the final operating condition is stable or not, and also provides information at intermediate points along the system trajectory [7].

## 2.2 System models

The ac system model is a transient stability model [6, 17, 18]. Generators may be modelled as voltage sources behind transient reactances with q-axis transient voltage dynamics included. For the transmission system a constant admittance model is used and a voltage and frequency dependent model is used for loads [12, 19]. HVDC

links are modelled assuming ideal harmonic filtering and balanced 3-phase operation [18, 23, 24, 25]. All the equations and details pertaining to system models can be found in [13].

Grouping all state variables defined by the differential equations of these models in a vector $\mathbf{z}$ , and all state variables defined by the algebraic equations in $\mathbf{u}$, the system model can be described by

$$\begin{aligned} \mathbf{M}\dot{\mathbf{z}} &= \mathbf{f}(\mathbf{z}, \mathbf{u}, \lambda) \\ \mathbf{0} &= \mathbf{g}(\mathbf{z}, \mathbf{u}, \lambda) \end{aligned} \tag{2.2}$$

where $\mathbf{f}(\cdot)$ represents a vector function of all right hand side of the differential equations, $\mathbf{g}(\cdot)$ groups all terms representing algebraic constraints, and $\mathbf{M}$ is a constant positive definite matrix.

When the algebraic constraints $\mathbf{g}(\cdot)$ have an invertible Jacobian $D_u\mathbf{g}(\cdot)$ along the system trajectories of interest, the algebraic variables can be eliminated by using the Implicit Function Theorem [20] and the system model can be reduced to

$$\mathbf{M}\dot{\mathbf{z}} = \mathbf{f}(\mathbf{z}, \mathbf{h}(\mathbf{z}, \lambda), \lambda) = \mathbf{s}(\mathbf{z}, \lambda) \tag{2.3}$$

A saddle-node bifurcation of the system (2.3) occurs when the Jacobian $D_z\mathbf{s}(\cdot)$ is singular at the equilibrium point $(\mathbf{z}_0, \lambda_0)$ where two solutions of the system, stable and unstable, merge and then disappear as the parameter $\lambda$ , i.e., the system load, changes.

Of all the possible types of local bifurcations characterized by a singular Jacobian at the equilibrium, i.e., saddle-node, transcritical, and pitchfork, only the saddle-node bifurcation occurs generically so that it is expected to be typical in practice [9, 10]. Then, under certain transversality conditions discussed in detail later, the behavior of equations (2.3) about the degenerate equilibrium point can be reduced to the following single variable one-parameter differential equation using a Lyapunov-Schmidt reduction [27, 28]:

$$\dot{x} = \lambda - x^2 = f(x, \lambda) \tag{2.4}$$

Figure 2.1 shows a diagram of the equilibria for $f(x, \lambda)$ as the parameter $\lambda$ changes. For $\lambda < 0$ equation (2.3) presents no equilibria, whereas for $\lambda > 0$ the vector field has stable and unstable equilibrium points. For the special case when $\lambda = 0$, the linearization of $f(x, \lambda)$ at the equilibrium (0,0) is singular, i.e., $\partial f/\partial x|_0 = 0$. Hence, the saddle-node is characterized by two equilibria coalescing and then disappearing as the parameter $\lambda$ changes. Notice also the quadratic shape of the bifurcation diagram

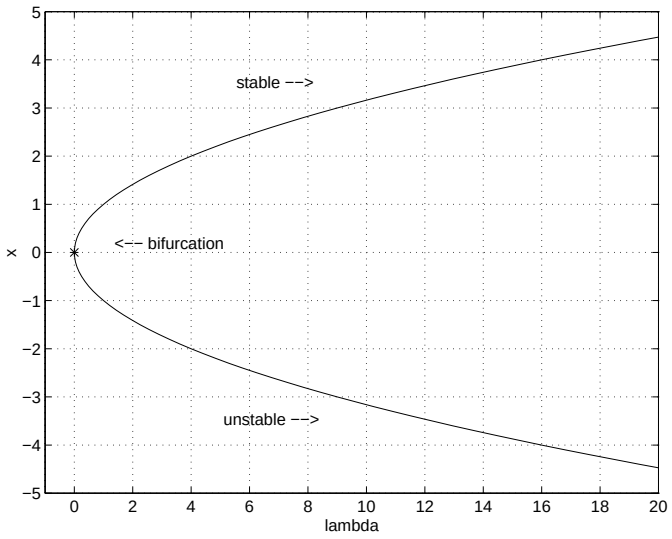


Figure 2.1: *Bifurcation diagram for* $f(x, \lambda) = \lambda - x^2$.

close to the degenerate equilibrium point, which is a characteristic of saddle-nodes that will be displayed in the behavior of actual ac/dc system bus voltage magnitudes when plotted versus a varying parameter $\lambda$ representing load change.

## 2.3 Equivalence of saddle-node equations [12]

Bifurcation studies for some power system models can be performed based on the eigenvalues of the power flow Jacobian, $\mathbf{J}_{PF}$, which can be shown to be singular at the same point where the Jacobian of the system dynamics $\mathbf{J}_{TS} = \mathbf{M}^{-1}\ D_z\mathbf{s}(\mathbf{z}_0, \lambda_0)$ becomes singular [6, 12, 13].

Linearizing $\mathbf{f}(\cdot)$ and $\mathbf{g}(\cdot)$ at the equilibrium point and eliminating the algebraic variables, the Jacobian for the reduced system is obtained

$$\mathbf{M}\ \mathbf{J}_{TS} = D_z\mathbf{f}|_0 - D_u\mathbf{f}|_0\ D_u\mathbf{g}|_0^{-1}\ D_z\mathbf{g}|_0 \tag{2.5}$$

which is shown in [12] to lead to

$$\det(D_z\mathbf{s}|_0) = (-1)^k \frac{\det \mathbf{J}_{PF}}{\det(D_u\mathbf{g}|_0)} \tag{2.6}$$

Therefore, zero eigenvalues of the enhanced power flow Jacobian indicate a singularity of the full linearized dynamics.

## 2.4 Zero eigenvectors

At the bifurcation point $(\mathbf{z}_0, \lambda_0)$, the Jacobian $D_z\mathbf{s}(\mathbf{z}_0, \lambda_0)$ has a simple and unique corresponding zero eigenvalue. The right eigenvector $\mathbf{v}$ associated to the zero eigenvalue and the left eigenvector $\mathbf{w}$ satisfy the following conditions :

1. $D_z\mathbf{s}(\mathbf{z}_0, \lambda_0)$ has a simple and unique zero eigenvalue, with normalized right eigenvector $\mathbf{v}$ and left eigenvector $\mathbf{w}$, i.e.,

$$\begin{aligned} D_z\mathbf{s}(\mathbf{z}_0, \lambda_0)\,\mathbf{v} &= \mathbf{0} \\ \mathbf{w}^T\, D_z\mathbf{s}(\mathbf{z}_0, \lambda_0) &= \mathbf{0}^T \end{aligned} \tag{2.7}$$

2. $$\mathbf{w}^T \left.\frac{\partial \mathbf{s}}{\partial \lambda}\right|_{(z_0, \lambda_0)} \neq 0. \tag{2.8}$$

3. $$\mathbf{w}^T \left[D_z^2\mathbf{s}(\mathbf{z}_0, \lambda_0)\,\mathbf{v}\right]\mathbf{v} \neq 0. \tag{2.9}$$

Conditions 1 through 3 guarantee generic quadratic behavior near the bifurcation point and are used to determine the collapse point [6, 15, 12].

The eigenvectors at the bifurcation point, provide information on the areas prone to voltage collapse and the control strategies to most efectively prevent this problem [11, 17].

Using a result from center manifold theory [21], the maximum absolute entry in $\mathbf{v}$ (the zero right eigenvector) shows which variable dominates in the Lyapunov-Schmidt reduction of the center manifold. This information is used in the prognosis of the system, i.e., it indicates which area is more prone to voltage collapse. Similarly, the maximum absolute entry in $\mathbf{w}$ (the zero left eigenvector) shows which derivatives are changing the most and is used to identify the most efficient control strategy to move away from the bifurcation [11, 17].

A similar approach is taken by the authors in [22], where the minimum singular value of the power flow Jacobian matrix is used as a static voltage stability index, and the right and left singular vectors are used to indicate sensitive voltages (and angles) and the most sensitive direction for changes of active and reactive power injections.

The continuation method [6], which is described in chapter 4, provides approximate right eigenvector information close to the bifurcation point; it also provides good initial guesses for the direct method [6, 17], which can be used for a more precise determination of the zero eigenvectors.

It is important to mention that, depending on the static load model used to represent the aggregated system loads, the location of a saddle-node bifurcation significantly changes. For example, for a constant P-Q load model one can show that the maximum power transfer point, or maximum loadability point, is a saddle-node bifurcation and it also corresponds to the tip of the P-V or "nose" curve [12].

# Chapter 3

# FACTS

## 3.1 Steady - state model for a SVC

### 3.1.1 Introduction and typical structure

Technology developments in power electronics together with sophisticated electronic control methods, have made the implementation of fast Static var Compensators (SVC) possible in the early 1970s. Today, there are hundreds of SVC installations, worldwide [29].

These devices are characterized by rapid response, wide operational range and high reliability. From the several possible approaches to generate and control reactive power, presently thyristor valves are used almost exlusively in conjunction with capacitor and reactor banks [29].

The main functionality of the SVC is to regulate the voltage at a chosen bus by controlling the reactive power injection at that location. Maintaining the rated voltage levels is important for proper operation and utilization of loads. Undervoltage causes degradation in the performance of loads such as induction motors, light bulbs, etc., whereas overvoltage causes magnetic saturation and resultant harmonic generation, as well as equipment failures due to insulation breakdown [29].

The maximum transmittable power for a simple two machine power system with ideal mid-point compensator is twice the steady-state power limit of the uncompen-

sated case [29]. This increase in the steady-state stability limit enhances the transient stability of the system. In addition to voltage regulation and transient stability improvement, the fast controls of the SVC allow for power oscillation damping.

All of the above contributed to the popularity of this device. Detailed, dynamical models are needed for transient stability studies; however, the steady-state behavior of the device can be completely described by a fundamental frequency model including controls and limits.

The most popular configurations of these shunt devices are the fixed capacitor with a thyristor controlled reactor (FC-TCR), and the thyristor switched capacitor, thyristor controlled reactor (TSC-TCR) [29]. From these two configurations, the second (TSC-TCR) is implemented in order to minimize standby losses and it is equivalent, from a steady-state perspective, to the FC-TCR. Therefore, the FC-TCR structure presented in Figure 3.1 is analyzed below.

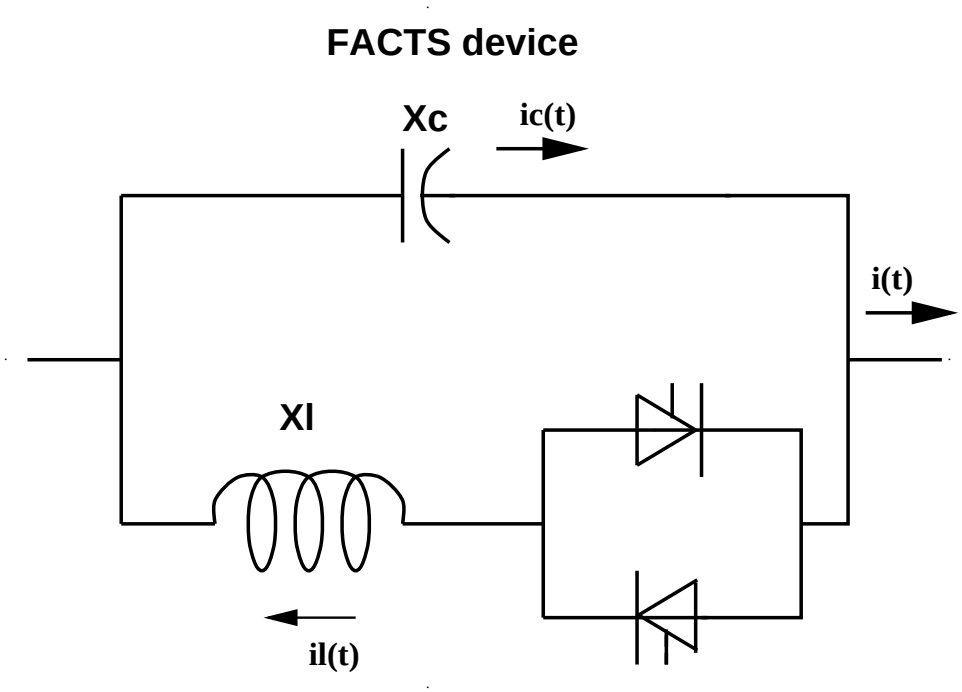


Figure 3.1: *Common structure for SVC and TCSC.*

### 3.1.2 The Thyristor Controlled Reactor (TCR)

The TCR consists of a fixed (usually air-core) reactor of inductance $L$ and a bidirectional thyristor valve (Figure 3.1). In a practical valve, many thyristors (typically 10 to 40) are connected in series to meet the required blocking voltage levels [29]. Applying simultaneously a gate pulse to all thyristors of a thyristor valve brings the valve into conduction. The valve will automatically block approximately at the zero crossings of the ac current, in the absence of a firing signal. Thus the controlling element is the thyristor valve.

The TCR current is essentially reactive, lagging the voltage by nearly 90°. The active component of the current is very small and the losses of the device are of the order of 0.5 – 2 % of the reactive power; therefore, one of the modelling assumptions is that the resistance of the inductor may be neglected. Another assumption that is made here is that the voltage applied to the TCR is sinusoidal, which for the SVC, a shunt device, is reasonable as the supply voltage is the bus voltage.

The firing angle $\alpha$ is defined as the angle in electrical degrees between the positive-going zero-crossing of the voltage accross the inductor and the positive going zero-crossing of the current through it. The thyristors are fired symmetrically; therefore, the maximum possible firing angle is 180°. Full conduction is obtained with a gating angle of 90°. Partial conduction is obtained with gating angles between 90° and 180°, with zero current at 180°. Firing angles less than 90° are not allowed, as they produce unsymmetrical currents with a high dc component. The fundamental component of the current is reduced as the firing angle increases [30]. This is equivalent to an increase in the inductance of the reactor, reducing its current as well as its reactive power.

In Figure 3.2, the voltage across the TCR inductor and the current through it are shown at full conduction angle. The current lags the voltage by 90° , both the current and the voltage being perfectly sinusoidal, the equivalent reactance of the TCR is equal to the inductor reactance $X_L$. In Figure 3.3 the current and voltage waveforms are shown for a firing angle of 120°. Only part of the sinusoidal voltage is applied to the inductor, the current and the voltage are not sinusoidal anymore. The fundamental component of the current is less than the current at 90° firing angle, resulting in an equivalent reactance of the TCR higher than $X_L$. Figure 3.4 shows the TCR current and voltage waveforms for a firing angle of 160°. The fundamental component of the current through the inductor is very small and, the equivalent reactance of the TCR is very high, at 180° it becomes practicaly infinite.

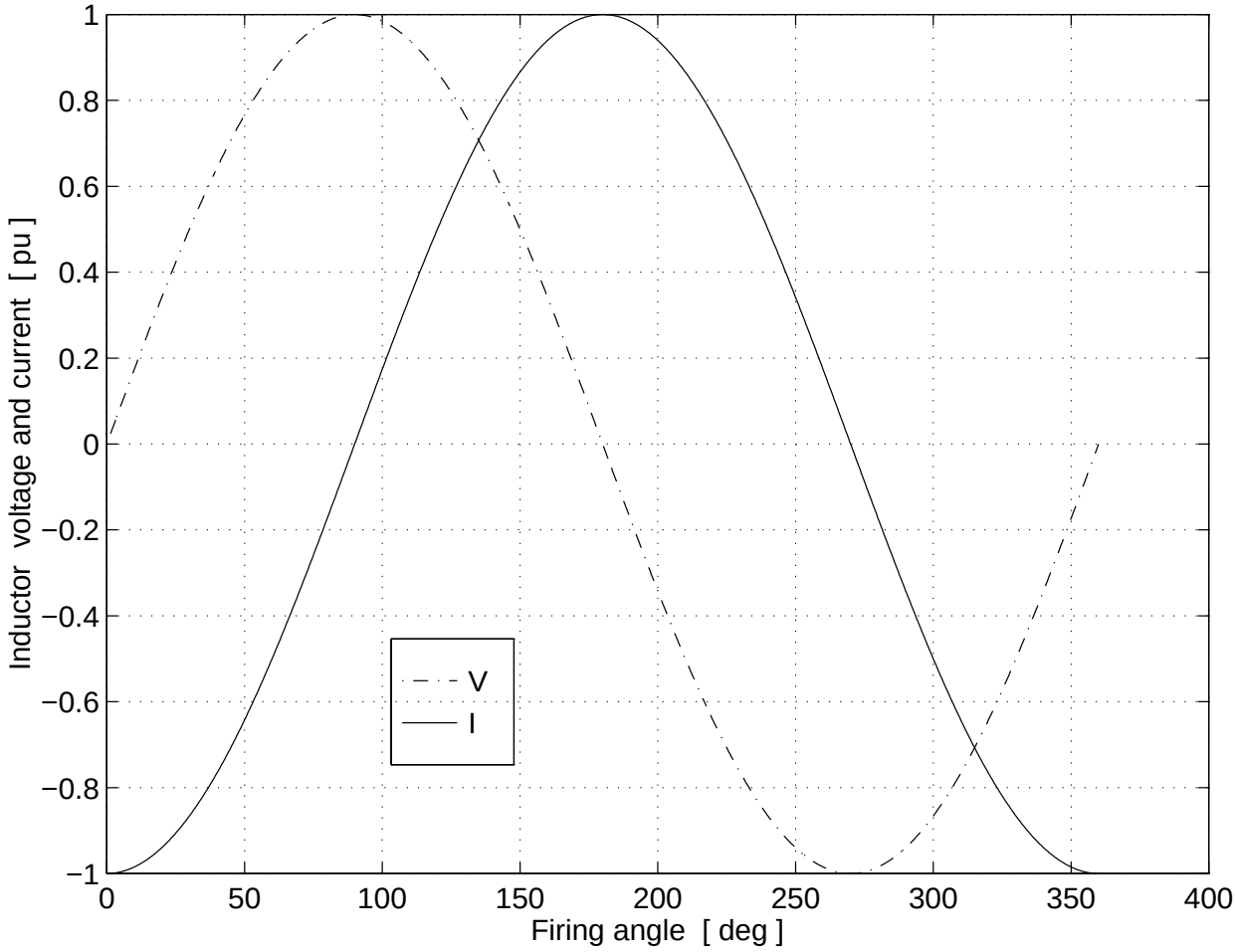


Figure 3.2: *Inductor current and voltage for* $\alpha = 90°$.

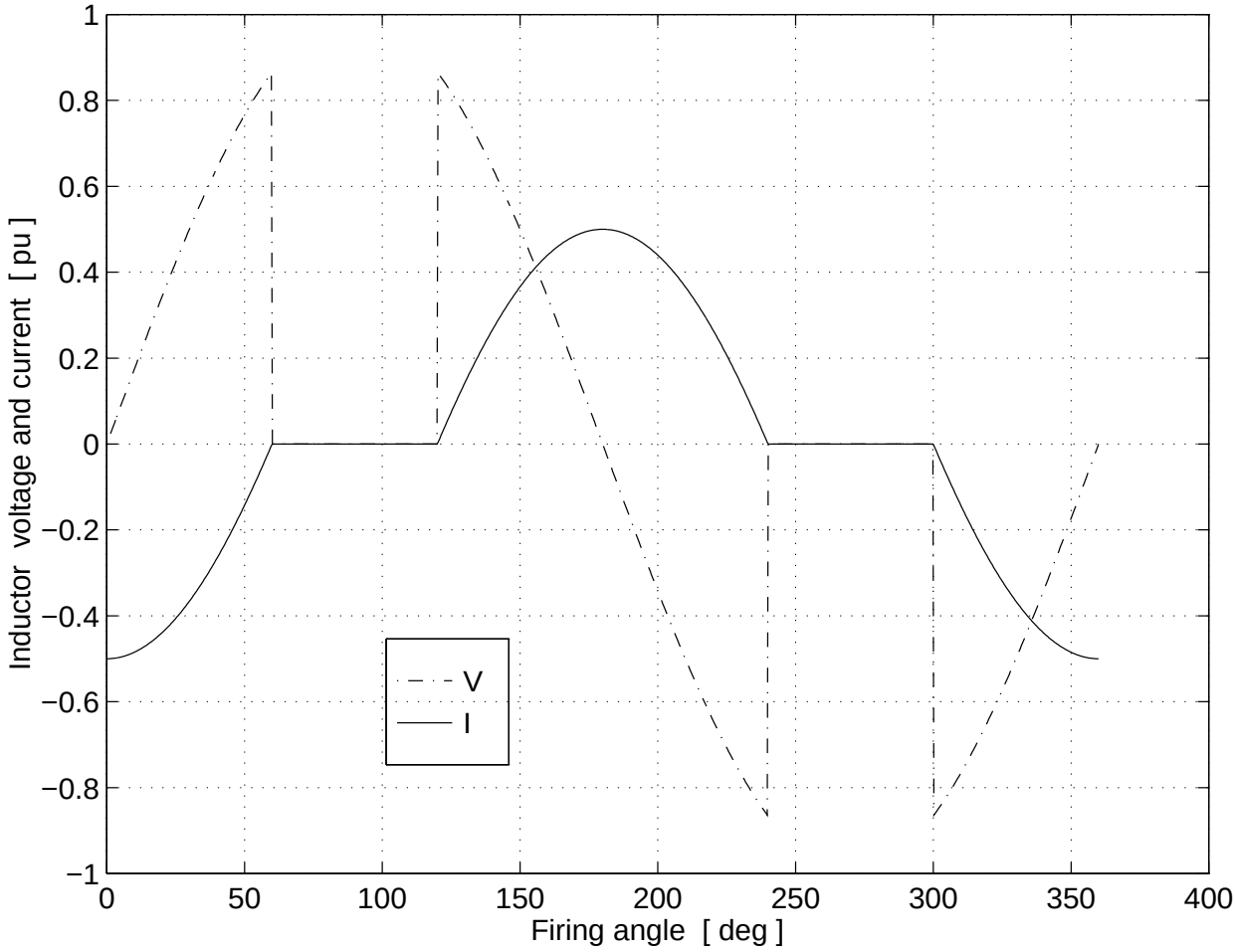


Figure 3.3: *Inductor current and voltage for* $\alpha = 120°$.

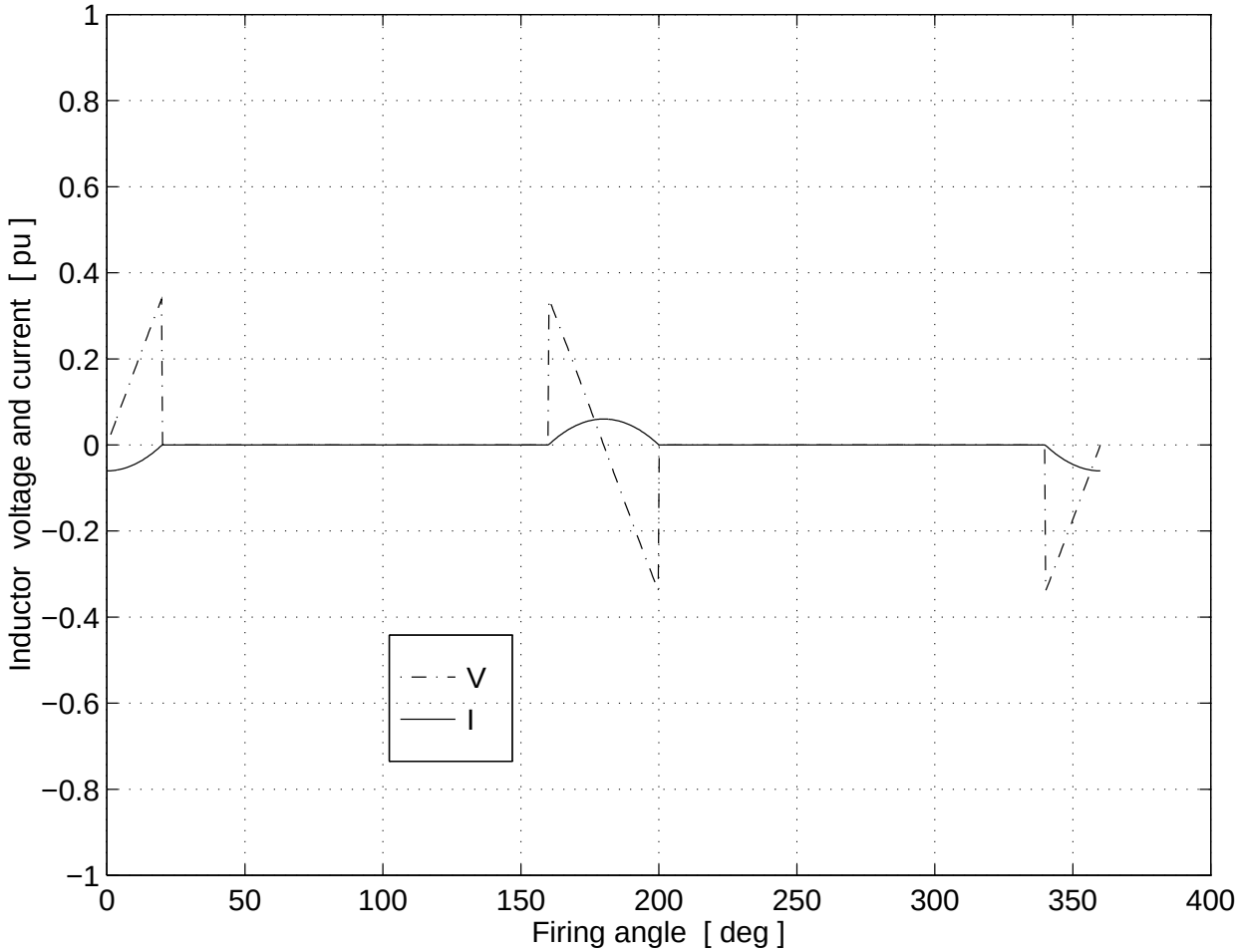


Figure 3.4: *Inductor current and voltage for* $\alpha = 160°$.

The conduction angle $\sigma$ is defined as the angle, in electrical degrees, for which the thyristor valve is conducting. The conduction angle $\sigma$ and the firing angle $\alpha$ are related by the following equation :

$$\sigma = 2\ (\pi - \alpha) \tag{3.1}$$

The steady-state voltage waveform for a period is described by Equation 3.2.

$$v_L(\omega t) \quad = \quad \begin{cases} V_M \sin \omega t & \text{for } 0 \leq \omega t \leq \pi - \alpha,\ \alpha \leq \omega t \leq 2\pi - \alpha,\ \pi + \alpha \leq \omega t \leq 2\pi \\ 0 & \text{for } \pi - \alpha < \omega t < \alpha,\ 2\pi - \alpha < \omega t < \pi + \alpha \end{cases} \tag{3.2}$$

The voltage across an inductor and the current through it are related by

$$v_L = L\frac{di_L}{dt} \tag{3.3}$$

If the time origin is chosen to coincide with a positive-going zero-crossing of the voltage, the current waveform can be found by integrating Equation 3.2 and it is analytically described by the equations in Table 3.1 [30], where $X_L$ is the fundamental frequency reactance of the inductor, $I_M = V_M/X_L$, is the maximum value of the inductor current, and $\omega = 2\pi f$, with $f$ being the fundamental frequency of the voltage waveform.

| $\omega t$ | $i_L(\alpha, \omega t)$ |
|---|---|
| $\omega t\ \epsilon\ [0, \pi - \alpha]$ | $I_M(-\cos\alpha - \cos\omega t)$ |
| $\omega t\ \epsilon\ [\pi - \alpha, \alpha]$ | $0$ |
| $\omega t\ \epsilon\ [\alpha, 2\pi - \alpha]$ | $I_M(\ \cos\alpha - \cos\omega t)$ |
| $\omega t\ \epsilon\ [2\pi - \alpha, \pi + \alpha]$ | $0$ |
| $\omega t\ \epsilon\ [\pi + \alpha, 2\pi]$ | $I_M(-\cos\alpha - \cos\omega t)$ |

Table 3.1: Inductor instantaneous current

where $X_L$ is the fundamental frequency reactance of the inductor, $I_M = V_M/X_L$, is the maximum value of the inductor current, and $\omega = 2\pi f$, with $f$ being the fundamental frequency of the voltage waveform.

A periodic function $f(\theta)$ with period $T$ can be expressed as a trigonometric Fourier series of the form [31] :

$$f(\theta) = \frac{A_0}{2} + \sum_{n=1}^{\infty}(A_n \cos n\theta + B_n \sin n\theta) \tag{3.4}$$

where

$$\begin{aligned} A_0 &= \frac{1}{\pi}\int_0^{2\pi} f(\theta)d\theta \\ A_n &= \frac{1}{\pi}\int_0^{2\pi} f(\theta)\cos n\theta d\theta \\ B_n &= \frac{1}{\pi}\int_0^{2\pi} f(\theta)\sin n\theta d\theta \end{aligned} \tag{3.5}$$

for $n \geq 1$.

Considering the analytical form of the inductor current, let $\theta = \omega t$. The TCR instantaneous current is a symmetric and even waveform; therefore, the corresponding Fourier series has $A_0 = 0$ and $B_n = 0$ for all $n$. For the steady-state model only the fundamental frequency term is considered, i.e.,

$$A_1 = \frac{1}{\pi}\int_0^{2\pi} i_L(\theta)\cos\theta d\theta \tag{3.6}$$

substituting for $i_L$ from Table 3.1

$$\begin{aligned} A_1 = \frac{I_M}{\pi}\Bigg[&-\cos\alpha\left(\int_0^{\pi-\alpha}\cos\theta d\theta - \int_\alpha^{2\pi-\alpha}\cos\theta d\theta + \int_{\pi+\alpha}^{2\pi}\cos\theta d\theta\right) - \\ &\int_0^{\pi-\alpha}\cos^2\theta d\theta - \int_\alpha^{2\pi-\alpha}\cos^2\theta d\theta - \int_{\pi+\alpha}^{2\pi}\cos^2\theta d\theta\Bigg] \end{aligned} \tag{3.7}$$

$$\tag{3.8}$$

After calculations, the final expression for $A_1$ is

$$A_1 = -\frac{I_M}{\pi}[2(\pi - \alpha) + \sin 2\alpha] \tag{3.9}$$

The fundamental frequency current laggs the voltage by $\frac{\pi}{2}$; hence, it can be written as

$$i_L(\omega t) = I_M \sin\left(\omega t - \frac{\pi}{2}\right) \tag{3.10}$$

Substituting $I_M$ in Equation (3.10) and expressing it as a cosine function, yields

$$i_L(\omega t) = -\frac{V_M}{X_V}\cos \omega t \tag{3.11}$$

From the Fourier series, and from Equation 3.11, the controllable reactance of the TCR, $X_V$, is then

$$X_V = X_L \frac{\pi}{2(\pi - \alpha) + \sin 2\alpha} \tag{3.12}$$

For design reasons that will be explained in the next section, let $X_L = 0.55X_C$. In this case, the reactance of the TCR, $X_V$, expressed in per unit with respect to $X_C$, the fixed capacitor reactance, is shown in Figure 3.5 as a function of the firing angle $\alpha$. At 90° the TCR is in full conduction and its equivalent reactance is equal to $X_L$. The inductive current flowing through the TCR is larger than the current through the capacitor; therefore, the device operates in the inductive region absorbing reactive power. At $\alpha = 113°$ the equivalent reactance of the TCR is equal to the capacitor reactance. For firing angles larger than 113°, the device operates in the capacitive region where the equivalent reactance of the TCR is larger than the capacitor reactance. At $\alpha = 180°$ the TCR reactance becomes practicaly infinite and the SVC injects the maximum reactive power.

In a three phase system, three single phase thyristor controlled reactors are used in delta connection. Under balanced conditions, the triplen harmonic currents (third, ninth, fiftenth, etc.) circulate in the delta connected TCRs and do not enter the power system. The magnitude of the other harmonics generated by the SVCs can be reduced by multiphase and multibank circuits or by filtering [29].

For the TCRs arranged in delta, the maximum Total Harmonic Distortion coeficient is less than 10 % [30]. A step down transformer is required in HV or EHV applications as the TCR voltage is limited for technical and economic reasons to 50 kV or below [32].

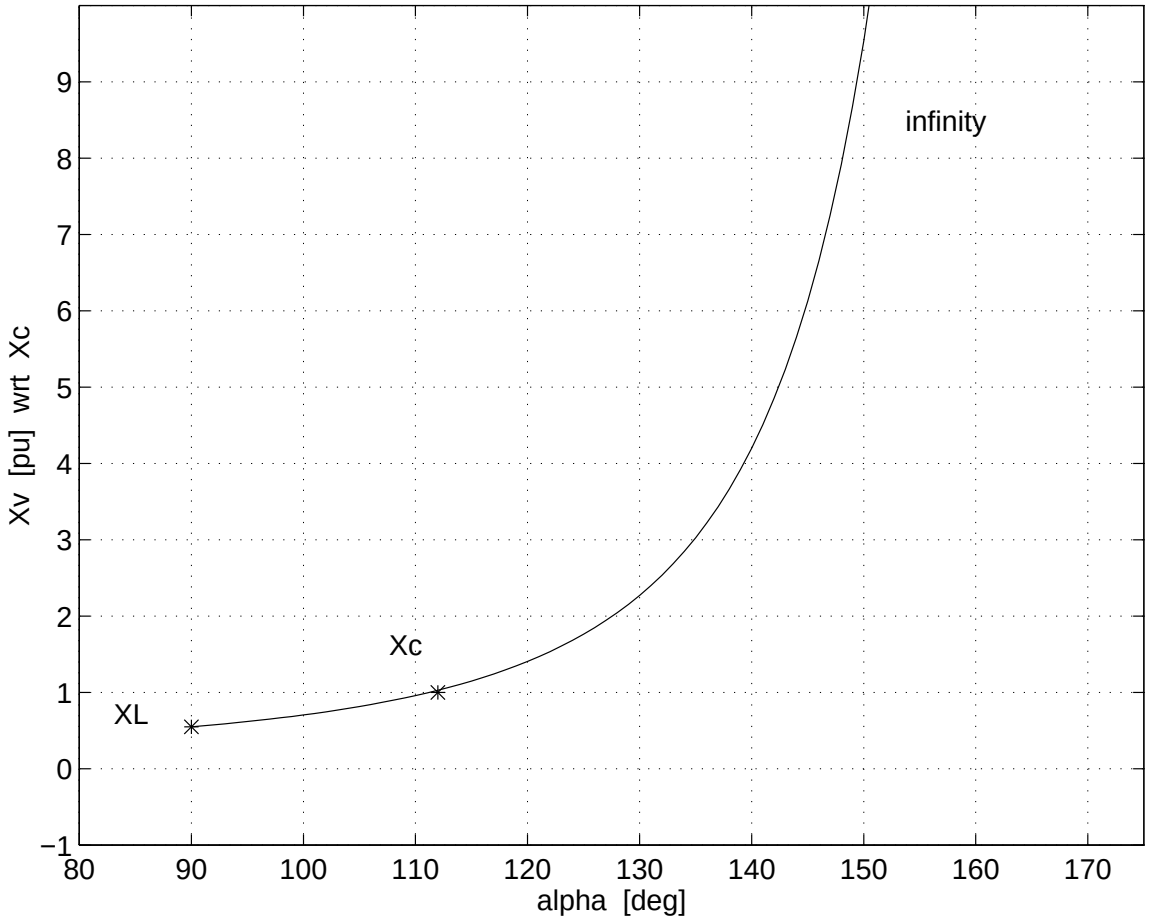


Figure 3.5: *TCR equivalent reactance.*

### 3.1.3 Control and limits of the SVC

The steady-state control law for the SVC is the typical current-voltage characteristic

$$V = V_{REF} + X_{SL} I \tag{3.13}$$

Typical values for the slope $X_{SL}$ are in the range of 0.02 to 0.05 p.u., with respect to the SVC base. The slope is needed to avoid hitting limits for small variations of the bus voltage. At the voltage limits, the SVC is transformed into a fixed reactance. A typical value for the controlled voltage range is 10 % [32, 33].

The V-I characteristic for the SVC is presented in Figure 3.6, where it is assumed that the capacitive and inductive range of the SVC are the same, and the SVC current is expressed in per unit with respect to the maximum current of the device (capacitive or inductive).

For the FC-TCR SVC, the reactive power of the device $Q_{SVC}$ can be written as

$$Q_{SVC} = \frac{V^2}{X_V} - \frac{V^2}{X_C} \tag{3.14}$$

At zero var output, the capacitive and inductive currents become equal and thus the capacitive and inductive var perfectly cancel each other. With a further decrease of the firing angle $\alpha$ (see Figure 3.5), the inductive current becomes larger than the capacitive current resulting in a net inductive var output.

From the V-I characteristic presented in Figure 3.6, the limits of the device are $\pm I_{Max}$ for $V$ varying from $V_{min}$ to $V_{Max}$, with $Q_{SVC}$ varying from $Q_{Max_C}$ to $Q_{Max_L}$. The typical model for the device is a reactive power source behind the slope reactance within $Q_{SVC}$ limits [32, 33]. The drawback of this approach is that it considers that the device hits the reactive power limits at the maximum/minimum voltage. However, the device is an adjustable reactance and the control limits are given by the firing angle limits. From Equation (3.14), it can be seen that if a firing angle limit is reached at a higher value of the voltage than the minimum controllable voltage (e.g., 0.95 p.u.), then the reactive power injected by the device is in fact higher than the maximum capacitive reactive power limit. Therefore, it is important in voltage collapse studies, where the system is stressed and devices are expected to hit limits, to consider the control limits, i.e., limits on the firing angle which are known, and not limits on the reactive power of the device which are voltage dependent.

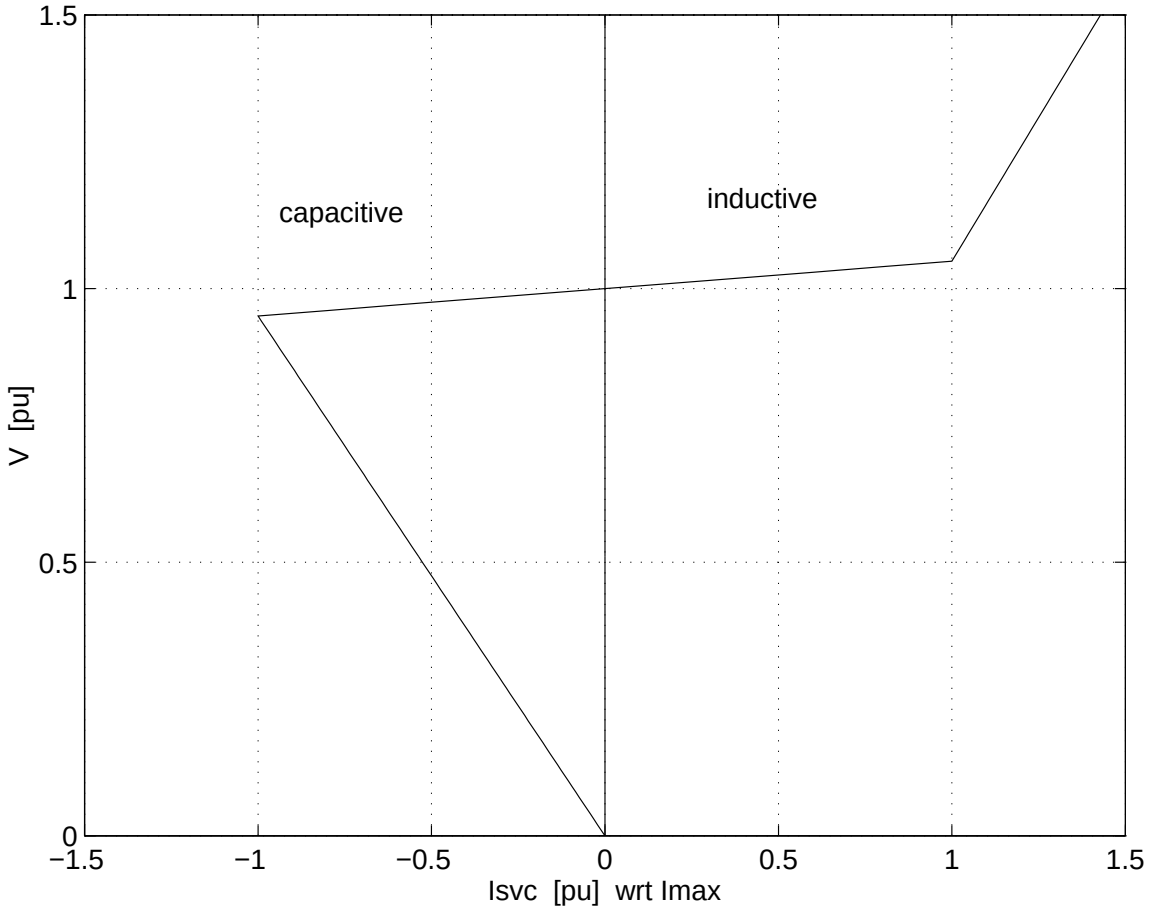


Figure 3.6: *SVC control characteristic.*

If the capacitive and inductive range are assumed to be equal for the SVC, i.e., $Q_{Max_C} = Q_{Max_L}$, with reactive power limits being reached at the voltage range limits, the reactive power limits are then given by

$$Q_{Max_C} = \frac{V_{min}^2}{X_C} \tag{3.15}$$

$$Q_{Max_L} = \frac{V_{Max}^2}{X_L} - \frac{V_{Max}^2}{X_C} \tag{3.16}$$

This equal power rating condition imposes a design constraint expressed by

$$X_L = 0.55 X_C \tag{3.17}$$

Alternatively one could consider equal current rating, i.e., $I_{Max_L} = I_{Max_C}$ at the voltage range limits, which results in the constraint

$$X_L = 0.53 X_C \tag{3.18}$$

Another option is to specify the inductive range of the SVC to be different from the capacitive range, as determined from power flow studies. In any of these cases, the ratings of the inductor and capacitor are similar if not equal. The SVC can be operated in steady-state in the capacitive or the inductive region; therefore, the ratings of the inductor and the capacitor are similar. For voltages higher than 50 kV the SVC needs to be connected to a step-down transformer. These two requirements are specific to the SVC and have to be considered in the total cost of the SVC system.

## 3.2 Steady-state model for a TCSC

### 3.2.1 Introduction and typical structure

In typical operation of power systems, the magnitude of bus voltages is generally controled to remain within maximum design limits and to prevent unacceptable voltage variations at the loads. For a certain power system, with fixed transmission impedances, the degree of power control by adjusting the voltage is limited. One has control over the power injected at generator buses and not on the angle between the bus voltages. This type of control is usually achieved by relatively slow changes

of rotor angles of synchronous machines, which is done by changing the mechanical power input at the shaft of the generators. Dynamic stability considerations usually limit the maximum permissible angles, and hence the transmitted power.

Shunt reactive devices have been used to increase power transfer capabilities. The most common shunt devices are mechanically switched shunt reactors and capacitors. Another shunt device allowing for a more versatile control of the voltage is the SVC.

Series capacitor compensation is another approach to improve stability limits and increase transfer capabilities. The transmitted power through a line is inversely proportional to the transfer impedance; thus, power transfer limits increase with the compensation of the line. For example, considering other parameters constant, 50 % series compensation approximately doubles the steady-state transmitted power, whereas 75 % series compensation would increase the transfered power to about four times the original value.

Despite the large improvement on transmittable power, high levels of series compensation are not typically used. The practical upper limit to the level of series compensation is about 70 % [8], as higher levels of steady-state compensation may generate uncontrollable variations in power for small changes in terminal voltages or angles, and large transient currents and voltages during disturbances at series resonant conditions.

In order to allow for the smooth variation of the series impedance in steady-state, a TCR is used in parallel with a conventional series capacitor. This type of scheme, called TCSC, has a capacitive and an inductive operating range. This type of installation was implemented at the Kayenta substation by the Western Area Power Administration (WAPA) in early 1992. The device is protected through the use of gapless metal oxide varistors (MOV), with by-pass breakers as a back-up protection [8].

From a steady-state perspective, the structure of the device is equivalent to a FC-TCR SVC presented in Figure 3.1. The main difference from a SVC is that the TCSC is series connected to the transmission line, whereas the SVC is shunt connected to a bus. Another major difference is that the TCSC is directly connected to the line, as opposed to the SVC which typically requires a step-down transformer. The rating of the device is also different; the inductive range of the TCSC is used only in transient operation where a bang-bang type of control is used to damp power oscillations; thus, the rating of the inductor is much lower than the rating of the capacitor.A relatively small (rating) device may be used to provide effective continuous control of the power on the ac line over a wide range.

As far as the fundamental components of the voltage and current are concerned, the TCSC is a controllable impedance given by the variable reactance of the TCR in parallel with the fixed capacitor. The equivalent impedance of the device is then

$$Z_e = jX_e$$

$$X_e = \frac{X_C X_L}{X_C/\pi[2(\pi-\alpha)+\sin 2\alpha] - X_L} \tag{3.19}$$

There is a value of the firing angle which causes steady-state resonance, i.e., $X_V = X_C$, this value is dependent on the ratio $r_x = X_C/X_L$. For example, Figure 3.7 depicts the equivalent reactance of the device for a ratio $X_C/X_L = 10$. The device can be continuously controlled in the capacitive or inductive zone, avoiding the steady-state resonance region; this type of control is called Vernier control.

### 3.2.2 Dynamical model and harmonics

In order to validate the steady-state model of the device, a dynamical model was developed. The simplified model of the Kayenta TCSC [8] is presented in Figure 3.8. An equivalent source $V_S$ supplies power to an ac transmission line modeled as a series $R_{line}$ and $X_{line}$ compensated by a TCSC with parameters $X_C$ and $X_L$. The equivalent voltage source represents the voltage drop across the compensated transmission line. This simplified model is used to study the effects of firing angle and compensation level on the harmonic content of the capacitor voltage $v_C$ and the line current $i_{line}$.

The thyristors were modelled as a nonlinear resistor $R_n$ controlled by the firing angle. The control synchronizes with the zero-crossings of the capacitor voltage and fires, i.e., $R_n =$ "*on*", at the given firing angle. The thyristors are switched off when the current drops below the value of the holding current. A state-space model was developed for this circuit using Kirchoff current and voltage laws (KCL and KVL), and choosing the capacitor voltage and the inductor currents as the state-space variables [34]. The state-space equations describing the circuit are presented below.

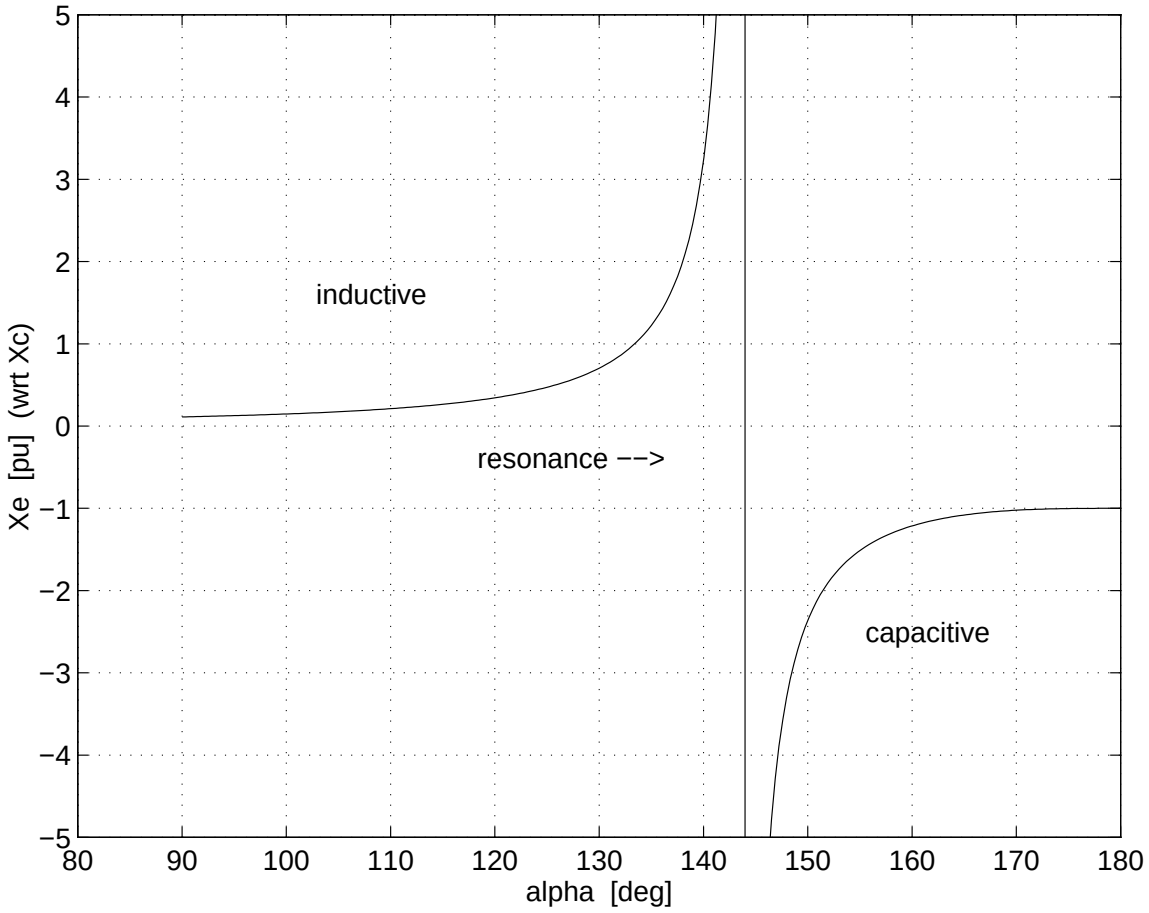


Figure 3.7: *Equivalent reactance of the TCSC.*

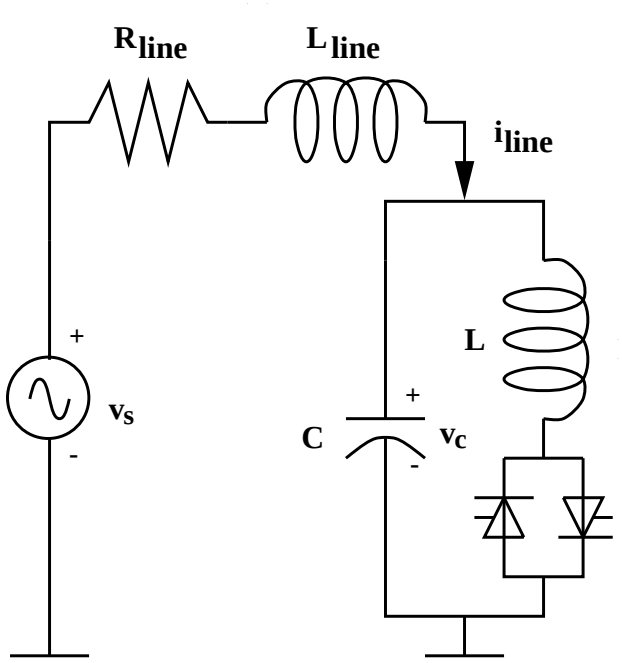


Figure 3.8: *Kayenta TCSC and line model.*

$$\begin{aligned}
\frac{dv_C}{dt} &= \frac{1}{C}i_{line} - \frac{1}{C}i_L \\
\frac{di_{line}}{dt} &= \frac{1}{L_{line}}V_M \sin \omega t - \frac{1}{L_{line}}v_C - \frac{R_{line}}{L_{line}}i_{line} \\
\frac{di_L}{dt} &= \frac{1}{L}v_C - \frac{R_n}{L}i_L \\
i_C &= i_{line} - i_L
\end{aligned} \tag{3.20}$$

The equivalent circuit used for the simulations is presented in Figure 3.9 with the following circuit parameters: $C = 176.84\ \mu F$, $R_n(on) = 0.001\ \Omega$, $R_n(off) = 1\ M\Omega$, $L = 6.8\ mH$, $R_{line} = 15.3\ \Omega$, $L_{line} = 153.8\ mH$, $V_M = 64.5\ kV$ and $\omega = 120\pi\ rad/s$. The steady state resonant point is reached at the value of $\alpha$ for which $X_V = X_C$, i.e., $\alpha_{res} = 136°$.

A damped trapezoidal integration method was implemented in order to handle the oscillations caused by the switching [35]. The control function was implemented within the integration method, since this provides easy access to the inputs, outputs

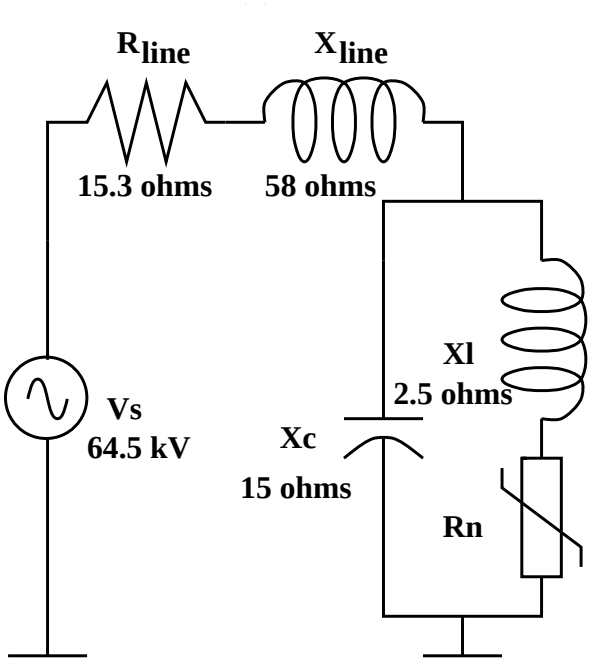


Figure 3.9: *Kayenta equivalent circuit.*

and states along the trajectory of the system. The chosen simulation environment was Matlab [36]. Typical waveforms for the inductive and capacitive region are presented in Figures 3.10, 3.11, 3.12, and 3.13.

The circuit was energized from zero initial conditions leading to switch-on dynamics during the first cycles. The transients settle down in 3 cycles for a firing angle in the inductive region, i.e., $\alpha = 120°$ (see Figure 3.10), whereas it takes about 8 cycles in the capacitive region with $\alpha = 160°$ (see Figure 3.12). Also, the values of the currents through the device and the line, and the capacitor voltage are considerably higher in the capacitive region. This suggests a start up strategy with the TCSC being energized in the inductive region and then brought into the capacitive region. For the inductive control, one can observe that the capacitor voltage is highly distorted (Figure 3.11) but the line current remains close to sinusoidal (Figure 3.10). In the capacitive region the capacitor voltage is almost undistorted (Figure 3.13) and the line current remains relatively free of harmonics (Figure 3.12). The capacitor takes a considerably higher current than the line current, which is an important constraint on the rating of the device. From the waveforms of the inductor, capacitor and line currents it can be seen that, for the capacitive region, the harmonic currents flow in a loop inside the device and the resulting line current is practically sinusoidal. In

Figure 3.13, the typical steady-state waveforms of the TCSC for a capacitive control are presented; these results are consistent with those presented in [8] for the Kayenta TCSC.

A harmonic analysis is done by using the Fast Fourier Transform (FFT) [31] on samples taken from the last cycle of the simulated time range, after the device reaches the steady-state region. The integration time step was chosen to be $\Delta t = 10^{-4}$, yielding 166 sample points per period. Harmonics higher than 30th are ignored by providing digital filtering to the high frequency numerical oscillations caused by the trapezoidal method. The THD is calculated for the line current and TCSC (capacitor) voltage from Equation (3.21) below [37].The simulation results are summarized in Table 3.2.

$$THD = \frac{1}{V_1}\sqrt{\sum_{n=2}^{30} V_n^2} \quad \% \tag{3.21}$$

| $\alpha\ [deg]$ | $THD_{I_{line}}$ [%] | $THD_{V_{TCSC}}$ [%] | $X_e$ |
|---|---|---|---|
| 100° | 2.3 | 29.9 | inductive |
| 120° | 2.7 | 48.7 | inductive |
| 130° | 3.9 | 43.7 | inductive |
| 140° | 16.2 | 27.9 | capacitive |
| 143° | 8.6 | 21.1 | capacitive |
| 150° | 2.5 | 11.3 | capacitive |
| 160° | 1.2 | 3.1 | capacitive |
| 170° | 1.7 | 1.8 | capacitive |
| 175° | 1.6 | 1.6 | capacitive |

Table 3.2: Total Harmonic Distortion factors for a TCSC

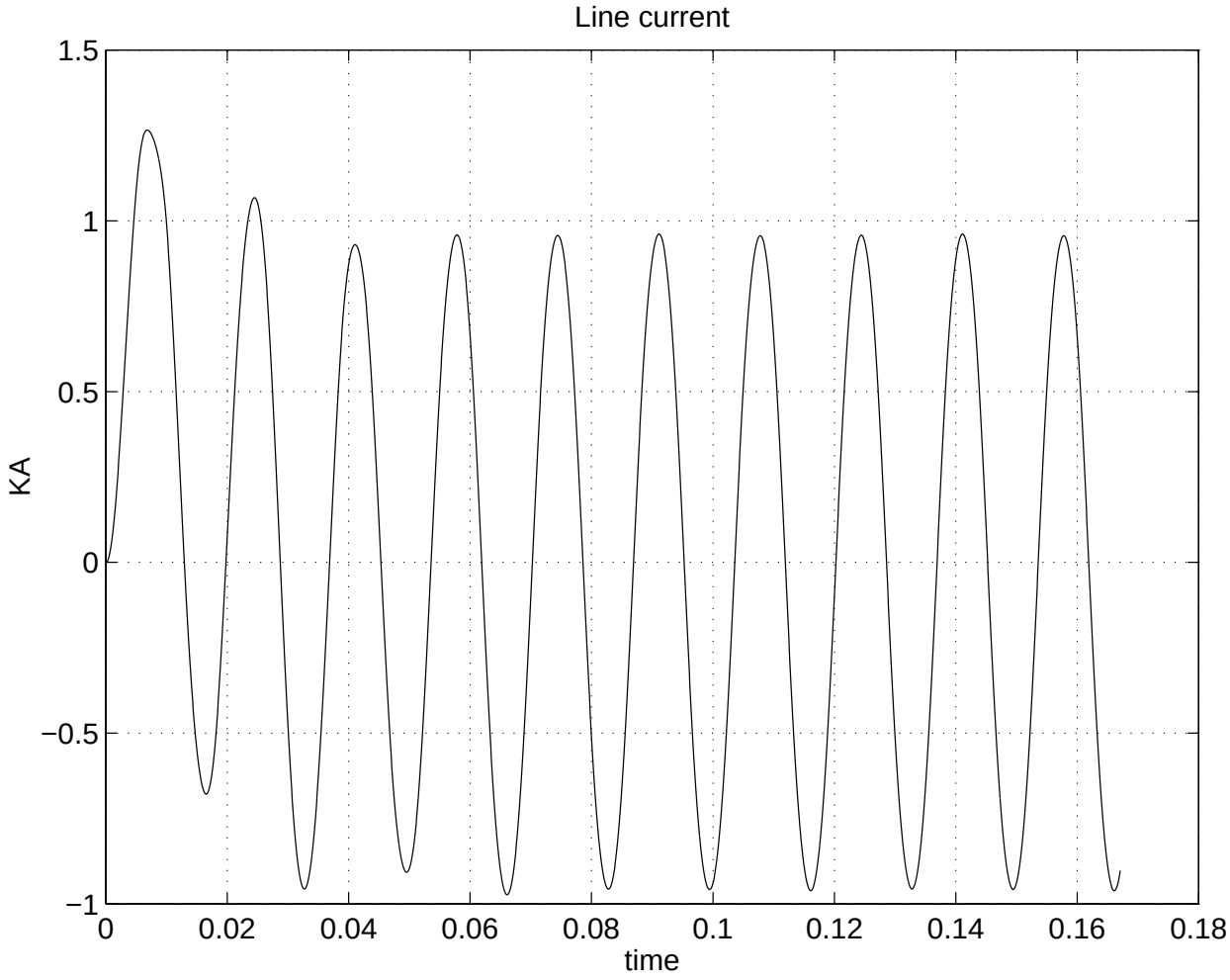


Figure 3.10: *Line current for* $\alpha = 120°$.

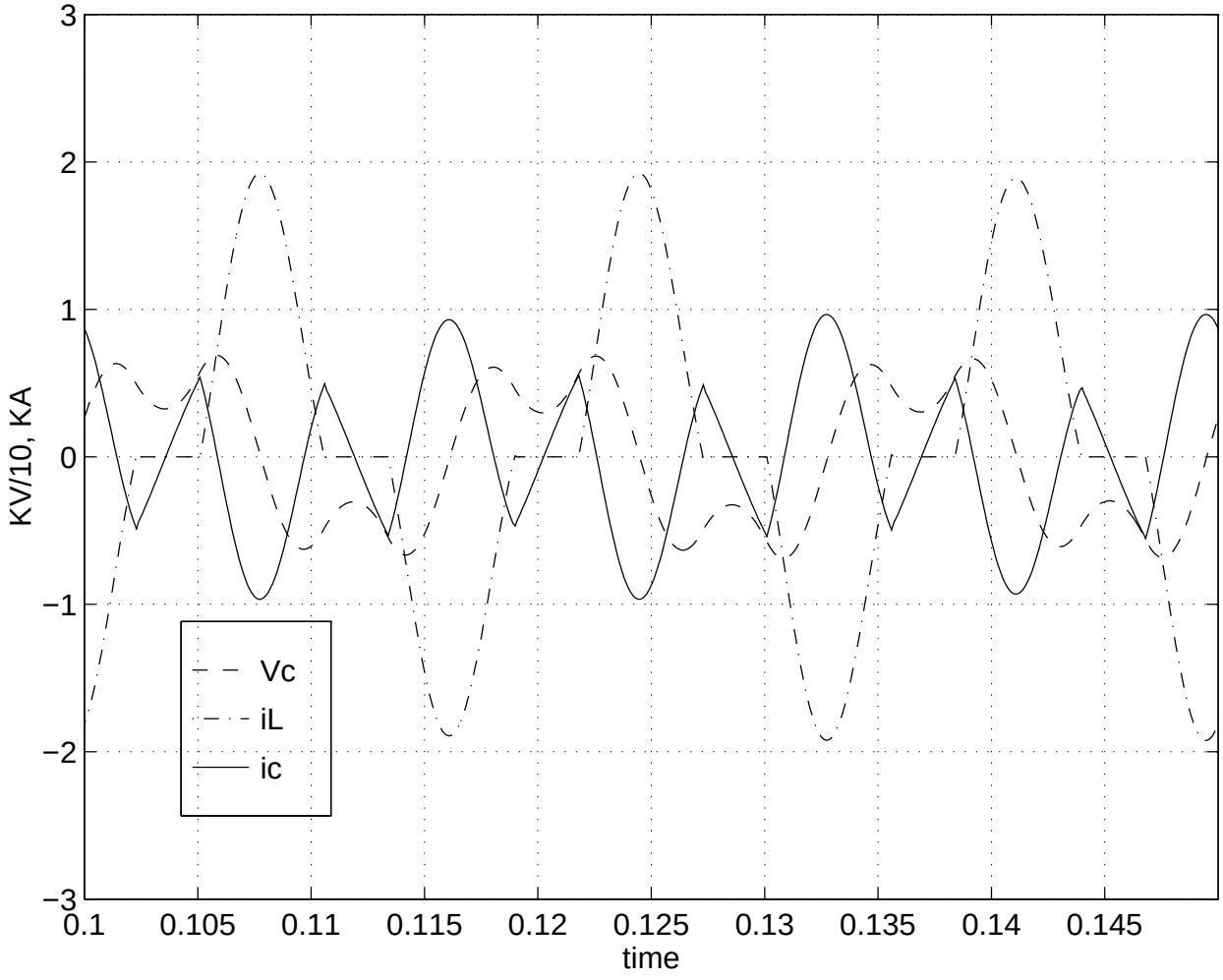


Figure 3.11: *Steady-state inductor current and capacitor voltage and current for* $\alpha = 120°$.

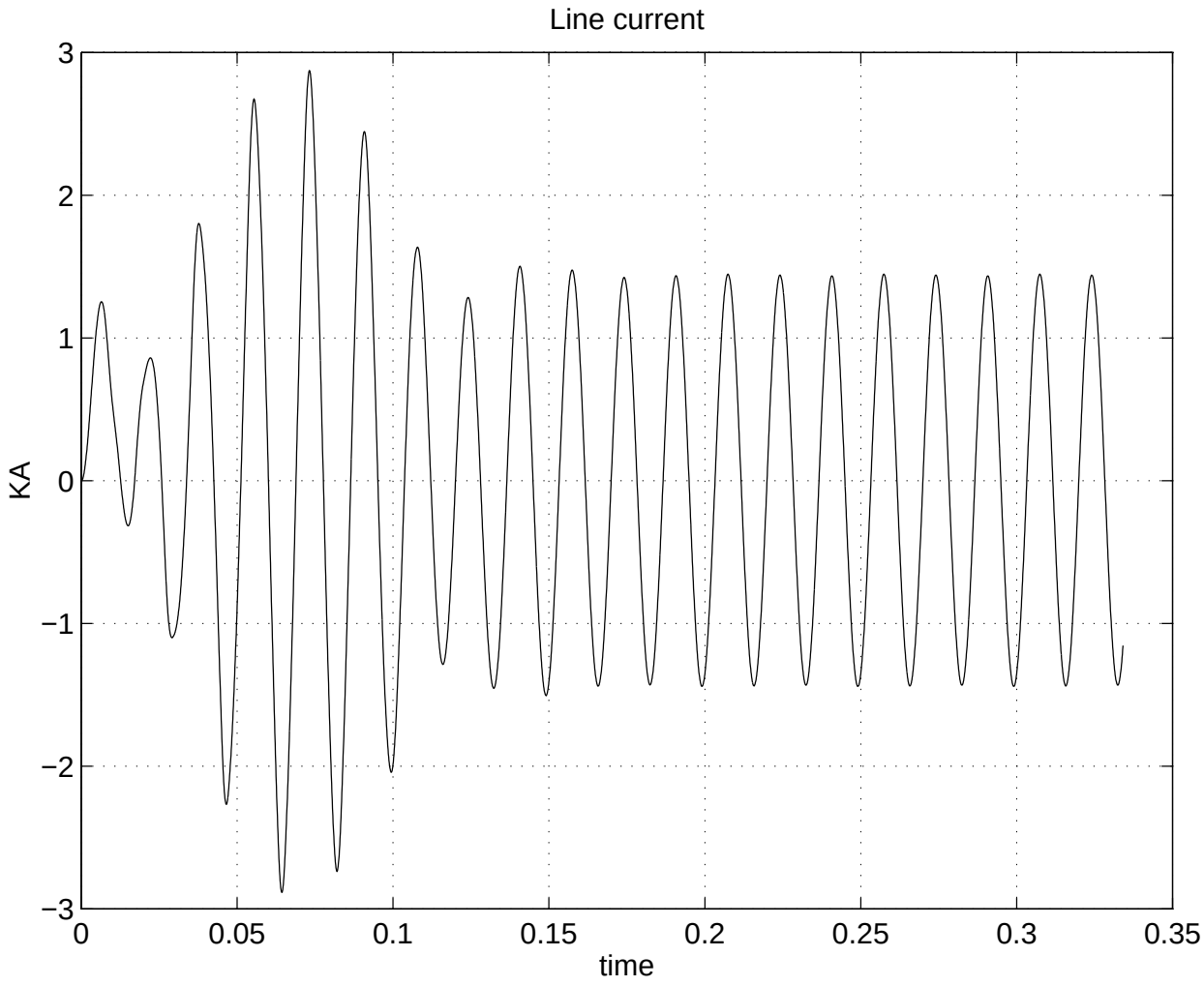


Figure 3.12: *Line current for* $\alpha = 160°$.

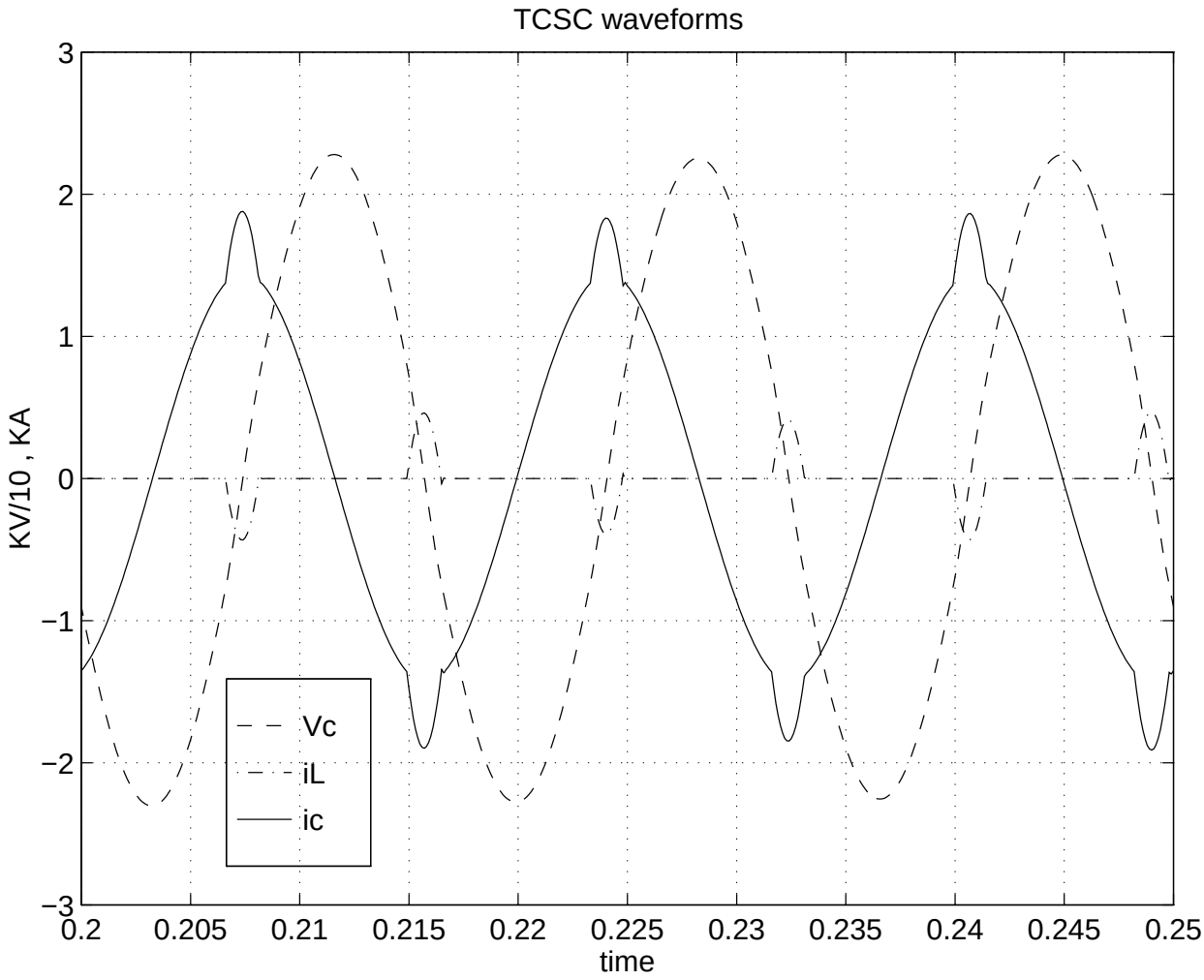


Figure 3.13: *Steady-state inductor current and capacitor voltage and current for* $\alpha = 160°$.

From Table 3.2, one observes that in the inductive region the TCSC current is almost undistorted (THD less than 5 %), whereas the TCSC voltage is higly distorted (THD more than 30 %). Close to the steady-state resonant point both the voltage and the current are highly distorted. At $\alpha = 143°$ the TCSC compensates 70 % of the line impedance, which is typically the highest level of compensation. At lower levels of compensation, the THD coefficient for both line current and TCSC voltage, is less than 5 %, with the line current being less distorted than the voltage across the device. Close to the steady-state resonant point the harmonics are considerably higher, and in the inductive region they reach unacceptable levels for steady-state operation. This is another reason why the inductive region is used only transiently. For the typical operation of the device, in the capacitive region, the voltage harmonics are low and can be neglected, validating the assumption that the capacitor voltage and line current are sinusoidal. Hence, the same steady-state model, i.e., a fixed capacitive reactance $X_C$ in paralell with a variable reactance $X_V$ can be used for the TCSC and the SVC.

### 3.2.3 Control strategies and limits

The power transmitted over a compensated ac line is primarily determined by the magnitude of line end voltages, the phase angle difference between them, and the equivalent line impedance. If one neglects the resistance of the line, which is typically the case for medium and long lines, the transmitted power can be expressed by

$$P = \frac{V_1 V_2}{X_e} \sin \theta_{12} \tag{3.22}$$

where $V_1$ and $V_2$ are the line end voltages, $X_e$ is the equivalent series reactance of the compensated line, and $\theta_{12}$ is the angular difference between the two line end voltages.

The typical control law for the TCSC is reactance modulation, for example at 70 % compensation

$$X_{TCSC} = 0.7 X_{line} \tag{3.23}$$

From Equation (3.22), it can be seen that in order to control power with fixed reactance control through the specified corridor, i.e., the compensated line, one would have to assume all of the parameters constant. Since the TCSC injects a certain amount of reactive power into the line, it will affect the voltages at both ends and the transmission angle. Therefore, the transmitted power will vary with these parameters.

An alternative to this control strategy is power modulation, i.e.,

$$P_{TCSC} = P_{set} \tag{3.24}$$

This control strategy allows the power system operators to specify a fixed amount of power to flow through the line. Another similar control strategy is current modulation (Equation (3.25)). This control mode allows the operation of the device close to the line thermal rating, since the controlled parameter is the line current.

$$I_{line} = I_{set} \tag{3.25}$$

Power and current modulation are typical transient control modes, used for power swing damping [8, 38].

Transmission angle modulation can be used to increase the stability of the system, by maintaining the angle at a low value. This control strategy is described by Equation (3.26).

$$\theta_{12} = \theta_{set} \tag{3.26}$$

The control mode can be switched from one law to another in order to maximize the capability of power transmission of the system. For example, from a constant compensation level, at a given loading of the line the control can be switched to constant transmission angle.

The control limits of the device are given by the firing angle limits. For the inductive region, which is not used in steady-state, acceptable values of the firing angle are between $\alpha_{min}$ and $\alpha_{max_L}$, where $\alpha_{min} = 90°$ and $\alpha_{max_L} < \alpha_{res}$, with the resonant value of the firing angle being determined by the ratio $r_x = X_C/X_L$, (Figure 3.7). The capacitive region is limited by $\alpha_{min_C}$ and $\alpha_{max}$, where $\alpha_{min_C} > \alpha_{res}$ and $\alpha_{max} = 180°$. The actual values of $\alpha_{max_L}$ and $\alpha_{min_C}$ depend on the ratio $r_x$ which determines the resonant point, and on the chosen margin to avoid resonance. Other factors such as recovery time after a fault will influence the operational limits.

# Chapter 4

# Power Flow

## 4.1 Introduction

The purpose of a power system is to deliver the required power to the customers, within acceptable voltage and frequency limits and in a reliable and economic manner. Since the reliability and economy of system operation are usually conflicting requirements, the analysis of the power system has to provide an optimal solution for a variety of conditions.

Power flow or load flow analysis is an important issue in system planning and operation, and it is the most common of power system computer calculations. In this analysis, the transmission system is modeled by a set of buses or nodes interconnected by transmission links. Generators and loads connected to various nodes of the system, inject and absorb power from the transmission system. The model considered in power flow studies is appropiate for finding the steady-state powers and voltages of the transmission system [39].

The ac/dc power flow problem consists of finding the equilibrium points of the differential-algebraic equations (DAE) briefly described in Chapter 2 (Equations 2.2). The problem can be reformulated as solving a system of nonlinear algebraic equations of the form:

$$\begin{cases} \mathbf{f}(\mathbf{x}_{ac}, \mathbf{y}_{dc}) &= \mathbf{0} \\ \mathbf{g}(\mathbf{x}_{ac}, \mathbf{y}_{dc}) &= \mathbf{0} \end{cases} \tag{4.1}$$

where $\mathbf{f}(\mathbf{x}_{ac}, \mathbf{y}_{dc}) = \mathbf{0}$ describes the ac network equations, $\mathbf{g}(\mathbf{x}_{ac}, \mathbf{y}_{dc}) = \mathbf{0}$ represents the dc system equations, $\mathbf{x}_{ac}$ is the vector of ac system variables and $\mathbf{y}_{dc}$ is the vector of dc system variables. There are basically two main approaches to solve this problem, the sequential approach and the unified approach.

The sequential approach starts with an initial guess $(\mathbf{x}^0_{ac}, \mathbf{y}^0_{dc})$ and keeping $\mathbf{y}^0_{dc}$ fixed, solves for $\mathbf{x}^1_{ac}$ from Equation $\mathbf{f}(\mathbf{x}_{ac}, \mathbf{y}_{dc}) = \mathbf{0}$, then solves for $\mathbf{y}^1_{dc}$ from Equation $\mathbf{g}(\mathbf{x}_{ac}, \mathbf{y}_{dc}) = \mathbf{0}$ with $\mathbf{x}^1_{ac}$ fixed. The method continues to solve one set of equations after the other with the initial guess given by the previous solution until it converges, i.e. both equations are satisfied within the specified precision. If $(\mathbf{x}^s_{ac}, \mathbf{y}^s_{dc})$ is the solution of the ac/dc system, the convergence criterion can be expressed by

$$\begin{aligned} \|\mathbf{f}(\mathbf{x}^s_{ac}, \mathbf{y}^s_{dc})\| &\leq \epsilon_{ac} \\ \|\mathbf{g}(\mathbf{x}^s_{ac}, \mathbf{y}^s_{dc})\| &\leq \epsilon_{dc} \end{aligned} \tag{4.2}$$

where $\epsilon_{ac}$ and $\epsilon_{dc}$ are the specified precision margins for the ac and dc equations.

The sequential method is used by commercial packages, such as CYMFLOW [40], mainly due to the fact that ac power flows were readily available and the method allows for the implementation of dc systems without major modifications to the ac solution. If the Newton-Raphson (N-R) method is used to solve the ac and dc set of equations, the computational cost of the factorization is of order $\frac{2}{3}n^3_{ac} + \frac{2}{3}n^3_{dc}$ for each ac/dc iteration [41]; the final cost is $\frac{2}{3}n_{iter}(n^3_{ac} + n^3_{dc})$, where $n_{ac}$ and $n_{dc}$ are the number of ac and dc equations and $n_{iter}$ is the number of iterations required by the method to converge.

The unified approach is to solve the system of equations simultaneously, that is to lump the ac and dc variables into a vector $\mathbf{z}$ and solve the system

$$\mathbf{s}(\mathbf{z}) = 0 \tag{4.3}$$

where $\mathbf{s}$ represents the ac/dc network equations. The system described by Equation 4.3 is solved using a N-R algorithm with initial guess $\mathbf{z}^0$ for the vector of system variables, i.e., voltages, angles, active and reactive powers and dc variables.

The N-R algorithm provides an approximate solution to the nonlinear problem described by Equation 4.3, by solving for $\mathbf{\Delta z}^i$ in the linear problem $\mathbf{J\Delta z}^i = -\mathbf{s}(\mathbf{z}^i)$, where $\mathbf{J} = D_z\mathbf{s}(\mathbf{z}^i)$. The method starts from an initial guess $\mathbf{z^0}$ and updates the solution at each step, i.e., $\mathbf{z}^{i+1} = \mathbf{z}^i + \mathbf{\Delta z}^i$, where i represents the step. This iteration scheme works if the initial guess is relatively close to the solution and the sequence of Jacobians evaluated at each iteration is not singular for any $i$ [39].

The computational cost of the factorization for the unified method is of order $\frac{2}{3}(n_{ac}+n_{dc})^3$; therefore, it depends on how many ac/dc iterations are necessary to compare the efficiency of the two methods. However, from a convergence point of view, the unified approach is superior because it has control over limits at each iteration and the interaction between the ac and dc systems is better represented. Another advantage of the unified approach is that new equations, for example equations representing FACTS devices, can be added to the original ac/dc set and the same numerical method (N-R) can be used to solve the enhanced system. Thus, the unified approach is the preferred method in this thesis.

## 4.2 Implementing FACTS devices in the power flow

The model used for the ac/dc system is briefly discussed in chapter 2. In this case the Jacobian of the ac/dc system, used by the N-R method, has the following structure

$$\mathbf{J} = \begin{array}{c} \\ f_1 \\ \vdots \\ f_{n_{ac}} \\ g_1 \\ \vdots \\ g_{n_{dc}} \end{array} \begin{array}{c} \begin{array}{cccccc} x_1 & \dots & x_{n_{ac}} & y_1 & \dots & y_{n_{dc}} \end{array} \\ \left[\begin{array}{ccc|ccc} & & & & & \\ & AC & & & & \\ & & & & & \\ \hline & & & & & \\ & & & & DC & \\ & & & & & \end{array}\right] \end{array} \tag{4.4}$$

FACTS devices are implemented in the power flow by lumping the equations describing their behavior with the ac/dc set. This will increase the dimensionality of the ac/dc Jacobian by $n_F$, where $n_F$ is the number of suplimentary system variables and equations introduced by the FACTS devices. The new structure of the system Jacobian is then

$$\mathbf{J} = \begin{array}{c|c|c|c} & x_1 \ \ldots \ x_{n_{ac}} & y_1 \ \ldots \ y_{n_{dc}} & r_1 \ \ldots \ r_{nF} \\ \hline f_1 \\ \vdots \\ f_n & AC & & \\ \hline g_1 \\ \vdots & & DC & \\ g_{n_{dc}} & & & \\ \hline F_1 \\ \vdots & & & FACTS \\ F_{nF} & & & \end{array} \tag{4.5}$$

where $\mathbf{r} = [r_1 \ldots r_{nF}]^T$ is the vector of all FACTS variables and $\mathbf{F}$ is the vector function of all FACTS equations.

### 4.2.1 SVC

The SVC steady-state model is presented in Chapter 3. Typically the SVC is connected to the transmission system bus through a step-down transformer, which will be treated similarly to the other transformers in the system. The SVC with its parameters is schematically presented in Figure 4.1. Typically the controlled voltage is $V_l$.

Equations 4.6 describe the SVC connected to bus $k$ with bus voltage $V_k$.

$$\begin{aligned} -V_{REF} - X_{SL}\left(V_k B_V - \frac{V_k}{X_C}\right) + V_l &= 0 \\ -\frac{V_k^2}{X_C} + V_k^2 B_V + Q_{SVC} &= 0 \\ -\pi X_L B_V + 2(\pi - \alpha) + \sin 2\alpha &= 0 \end{aligned}$$

where $B_V = 1/X_V$.

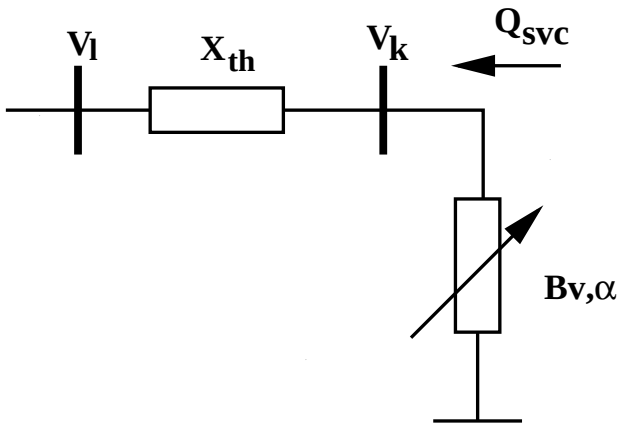


Figure 4.1: *SVC connected to the system.*

where the three additional SVC variables are $r_{SVC} = [Q_{SVC}\ B_V\ \alpha]^T$. Equations (4.6) can be represented as $\mathbf{F}_{SVC}(\mathbf{r}_{SVC}) = 0$, and the Jacobian structure is then

$$\mathbf{J} = \begin{array}{c|cccccc} & \cdots & V_k & \cdots & V_l & \cdots & Q_{SVC} \quad B_V \quad \alpha \\ \vdots & & & & & & \\ \Delta Q_k & & AC/DC & & & & X \\ \vdots & & & & & & \\ \hline F_{SVC1} & & X & & X & & \quad X \\ F_{SVC2} & & X & & & & X \quad X \\ F_{SVC3} & & & & & & \quad X \quad X \end{array} \tag{4.6}$$

where $X$ stands for a nonzero SVC Jacobian entry.

The initialization of the SVC variables in the N-R routine is done either from a "flat start" or from a user defined initial guess. The "flat start" is based on the initial values of ac variables and the equivalent reactance characteristic (Figure 3.5). Since for $X_V = X_C$, $Q_{SVC} = 0$, this is a valid starting point. The firing angle $\alpha$ is initialized at 92°, which provides good results for test systems, i.e., convergence, for the base load and other loading conditions. Therefore, $\mathbf{r}^0_{SVC} = [Q^0_{SVC}\ B^0_V\ \alpha^0]^T = [0\ 1/X_C\ 1.606]^T$, $\alpha$ in radians. Notice that the susceptance of the TCR, $B_V$, is used instead of its reactance, $X_V$; this is due to better numerical properties of the SVC equations with respect to $B_V$ (Figure 4.2), as $B_V$ varies between $1/X_L$ and 0, whereas $X_V$ varies between $X_L$ and infinity (Figure 3.5).

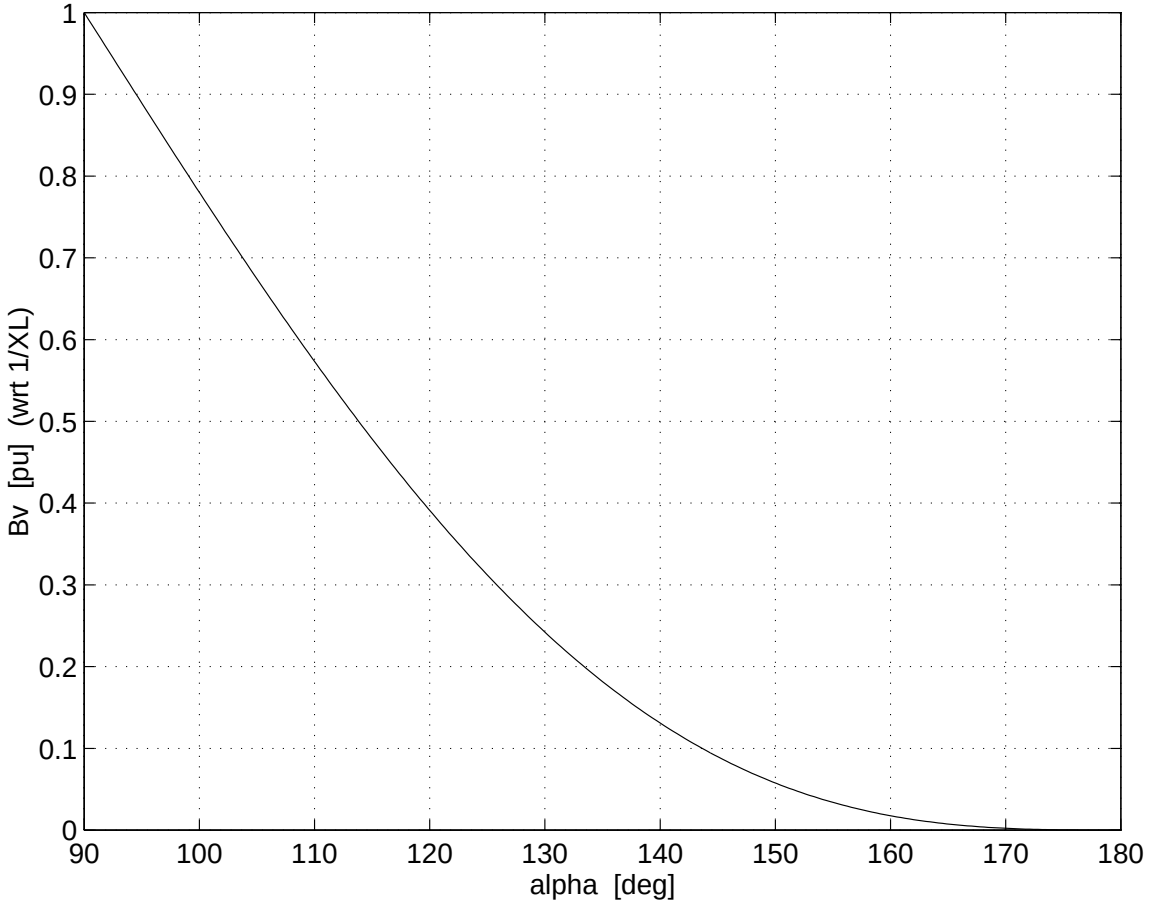


Figure 4.2: *SVC equivalent susceptance.*

A "WSCC type" format is proposed for the SVC power flow input data in Appendix A. This format is consistent with the WSCC format [42], allowing the user to specify the location, the structure and the control characteristics and limits of the SVC.

SVC limits are considered as limits on the firing angle $\alpha$, i.e., $\alpha\epsilon[\alpha_m, \alpha_M]$, where $\alpha_m$ is the minimum firing angle and $\alpha_M$ is the maximum firing angle. If there is no solution within the limits for $\alpha$, the firing angle is fixed at that limit and $V_{REF}$ becomes a variable. This procedure, depicted in Figure 4.3, allows for the use of the same set of equations when the SVC is at its limits. Moreover, by calculating the additional variable $V_{REF}$ when $\alpha$ hits a limit, the SVC may regain control of the voltage if the interaction with the rest of the system brings $V_l$ within the controlable region.

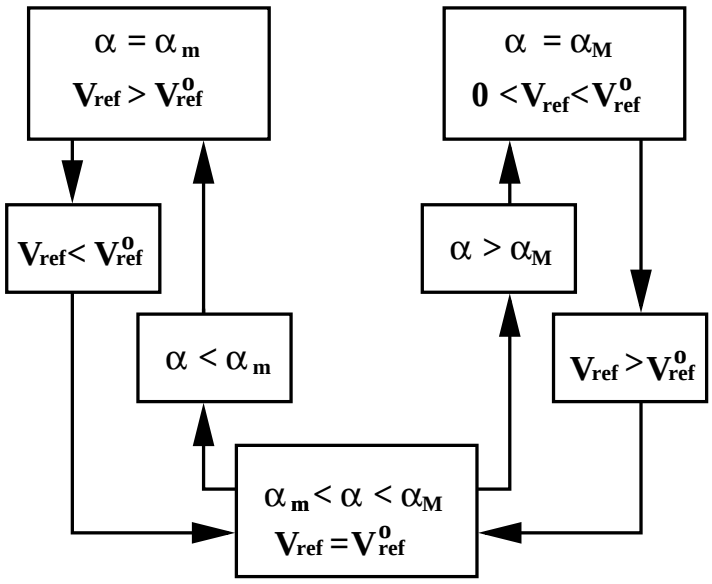


Figure 4.3: *Handling of SVC limits.*

### 4.2.2 TCSC

The TCSC steady-state model is discussed in Chapter 3. The TCSC is assumed to be connected between buses $k$ and $m$ (Figure 4.4). The device model is lossless; thus, the active power $P$ injected in the TCSC from node $k$ is equal to the power injected by the device in node $m$. The device is then represented by the following set of equations:

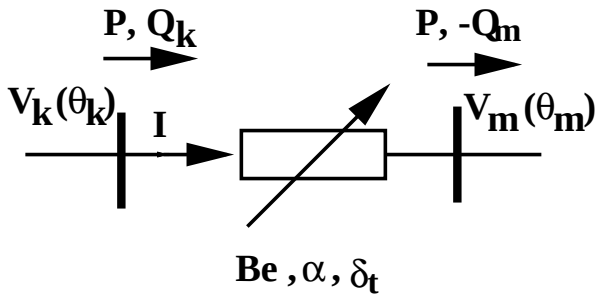


Figure 4.4: *TCSC between buses k and m.*

$$
\begin{aligned}
-V_k V_m B_e \sin(\theta_k - \theta_m) - P &= 0 \\
-V_k^2 B_e + V_k V_m B_e \cos(\theta_k - \theta_m) - Q_k &= 0 \\
-V_m^2 B_e + V_k V_m B_e \cos(\theta_k - \theta_m) - Q_m &= 0 \\
\frac{1}{X_C} - \frac{(2\pi - 2\alpha + \sin 2\alpha)}{\pi X_L} - Be &= 0 \\
\sqrt{P^2 + Q_k^2} - IV_k &= 0 \\
\theta_k - \theta_m - \delta_t &= 0
\end{aligned}
\tag{4.7}
$$

where $B_e = 1/X_e$. The control mode is defined by either one of the following equations:

- Constant reactance control

$$X_{SET} - X_e = 0$$

- Constant power control

$$P_{SET} - P = 0$$

- Constant current control.

$$I_{SET} - I = 0$$

- Constant transmission angle control.

$$\delta_{SET} - \delta_t \;=\; 0$$

seven additional TCSC variables form a vector of variables $\mathbf{r}_{TCSC}$, where $\mathbf{r}_{TCSC} = [P\ Q_k\ Q_m\ B_e\ \alpha\ I\ \delta_t]^T$. Similarly as for the SVC, the equivalent susceptance of the device is used rather than the equivalent reactance. Equations 4.8 may be written in the form $\mathbf{F}_{TCSC}(\mathbf{r}_{TCSC}) = 0$. The structure of the system Jacobian for all control laws is presented below

| | $\ldots$ | $\theta_k$ | $\ldots$ | $\theta_m$ | $\ldots$ | $V_k$ | $\ldots$ | $V_m$ | $P$ | $Q_k$ | $Q_m$ | $B_e$ | $\alpha$ | $I$ | $\delta$ |
|---|---|---|---|---|---|---|---|---|---|---|---|---|---|---|---|
| $\vdots$ | | | | | | | | | | | | | | | |
| $\Delta P_k$ | | | | | | | | | $X$ | | | | | | |
| $\vdots$ | | | | | | | | | | | | | | | |
| $\Delta P_m$ | | | | | | | | | $X$ | | | | | | |
| $\vdots$ | | | | | $AC$ | / | $DC$ | | | | | | | | |
| $\Delta Q_k$ | | | | | | | | | | $X$ | | | | | |
| $\vdots$ | | | | | | | | | | | | | | | |
| $\Delta Q_m$ | | | | | | | | | | | $X$ | | | | |
| $\vdots$ | | | | | | | | | | | | | | | |
| $F_1$ | | $X$ | | $X$ | | $X$ | | $X$ | $X$ | | | $X$ | | | |
| $F_2$ | | $X$ | | $X$ | | $X$ | | $X$ | | $X$ | | $X$ | | | |
| $F_3$ | | $X$ | | $X$ | | $X$ | | $X$ | | | $X$ | $X$ | | | |
| $F_4$ | | | | | | | | | | | | $X$ | $X$ | | |
| $F_5$ | | | | | | $X$ | | | $X$ | $X$ | | | | $X$ | |
| $F_6$ | | $X$ | | $X$ | | | | | | | | | | | $X$ |
| $F_7$ | | | | | | | | | $X$ | | | $X$ | | $X$ | $X$ |

(4.8)

where nonzero TCSC Jacobian entries are represented by $X$.

The initialization of the TCSC variables ("flat start") is based on its design constraints, the equivalent reactance characteristic and the firing angle limits. The TCSC initial guess uses an initial value of 2.6 radians for $\alpha$ and calculates the rest of the TCSC variables based on the initial values of the ac variables and Equations 4.8. The initial value of the firing angle was determined such that it is not close to the

limits. This initial guesses provide a robust starting point for a wide range of loading conditions. The range for $P_{SET}, I_{SET}$ and $\delta_{SET}$ can be obtained from preliminary power flow studies performed with different compensation levels.

TCSC limits are considered as limits on the firing angle $\alpha$. If $\alpha$ hits a limit, the firing angle is fixed at that limit and the control mode is switched to reactance control. The compensation level is given by the TCSC reactance at that firing angle.

Similarly to the SVC, a "WSCC type" format is proposed for the TCSC input data, as shown in Appendix A; it allows the user to specify the location, the structure, the control law and limits for the TCSC.

## 4.3 Continuation Power Flow [6]

For a given operating point and load increase direction, the loadability margin of a system is defined as the amount of power, in MW, that the system can supply before it undergoes voltage collapse. Assessing the loadability margin with conventional power flows has two major drawbacks: first it needs manual intervention, i.e., running a series of power flows with modified loads, and second, the steady-state voltage collapse point is determined by the nonconvergence of the conventional power flow. This nonconvergence is associated with the power flow Jacobian becoming singular; however, near the singularity point the Jacobian is almost singular, causing numerical problems. Therefore, the maximum loadability point depends on the method used, the specified error margin, and the maximum number of iterations. Thus, it is to be expected that results obtained with different power flow programs would be different, and one can not be sure about the precise location of the voltage collapse point. The determinant of the power flow Jacobian is highly nonlinear with respect to the loading factor [43]; therefore, conventional power flows cannot determine the voltage collapse point. Furthermore, right and left eigenvectors can be used to determine the most sensitive bus and the most efficient control strategy to avoid voltage collapse only if they are associated to the zero eigenvalue of the Jacobian at the exact singularity point. In [43] the authors show that the critical bus, i.e., the one associated with the minimum eigenvalue of the system, changes location with system loading. All of this further indicates the need for a precise determination of the voltage collapse point, which cannot be done with power flow programs only.

Continuation methods are typically used to determine the proximity to saddle-node bifurcations in dynamic systems; a thorough description can be found in [9].

Continuation power flows trace the solution of the power flow equations $\mathbf{s}(\mathbf{z}, \lambda) = 0$, where the parameter $\lambda$ stands for the loading factor. A continuation power flow is presented in [6] and [16]. The method can be summarized in three steps:

1. *Predictor:* Given an initial operating point find the next point in system variables and parameter space by choosing the tangent to the system trajectory and a step length. Mathematically this can be expressed by solving for the tangent $dz/dp$, $\Delta z$ and $\Delta p$ in

$$\begin{aligned} D_z\mathbf{s}(\mathbf{z}_0, p_0)\frac{d\mathbf{z}}{dp} &= -\left.\frac{\partial \mathbf{s}}{\partial p}\right|_0 \\ \Delta p &= \frac{k}{\|dz/dp\|} \\ \Delta z &= \Delta p \frac{dz}{dp} \end{aligned} \tag{4.9}$$

   where $D_z\mathbf{s}(\mathbf{z}_0, p_0)$ is the system Jacobian calculated at the initial point, and $\partial \mathbf{s}/\partial p|_0$ is the vector of partial derivatives of the system equations with respect to the parameter $p$. The parameter $p$ is set initially to $\lambda$ and $k$ is typically set to 1; as the bifurcation point is approached, $p$ is changed according to step 3.

2. *Corrector:* Using as the starting point the solution of the previous step (predictor), find the intersection between the perpendicular plane to the tangent vector and the system solutions trajectory, i.e., solve equations

$$\begin{aligned} \mathbf{s}(\mathbf{z}, p) &= 0 \\ \Delta p(p - p_0 - \Delta p) + \mathbf{\Delta z}^T(\mathbf{z} - \mathbf{z_0} - \mathbf{\Delta z}) &= 0 \end{aligned} \tag{4.10}$$

   where $\Delta p$ and $\mathbf{\Delta z}$ come from the predictor, and the initial guesses for $\mathbf{z}$ and $p$ are $\mathbf{z_0} + \mathbf{\Delta z}$ and $p_0 + \Delta p$. If a solution can not be found, the steps $\mathbf{\Delta z}$ and $\Delta p$ are cut in half until convergence is reached.

3. *Parameterization:* Checking the relative change in all the system variables, $p$ is interchanged with the variable that presents the largest variation. That is,

$$p \leftrightarrow max\left\{\left\|\frac{\Delta z_i}{z_i}\right\|, \left\|\frac{\Delta p}{p}\right\|\right\} \tag{4.11}$$

for $i = 1 \ldots n$.

The Jacobian of Equations 4.10 is nonsingular at the voltage collapse point, even for $p = \lambda$ [6, 12]. The method goes around the bifurcation point, allowing to trace the "unstable side" of the solution trajectory.

The continuation method presented above is implemented in a robust power flow program called PFLOW [17], using portable C code. The program reads WSCC [42], EPRI [25] and Common Format [44] input files and produces a variety of ASCII files, according to user defined options. It uses a N-R iterative process with automatic step-size adjustement to solve the ac/dc power flow. The factorization routines were taken from the Sparse Matrix Manipulation System (SMMS) [45]. The voltage collapse point for any given system can be determined with a variety of operational limits.

# Chapter 5

# Placement and design of FACTS

## 5.1 Location of FACTS

A 12 bus ac system [6] is used to study a methodology for the placement and design of a SVC and then a TCSC. The test system is presented in Figure 5.1, where the slack bus is considered to be bus 11.

The behavior of the system is investigated with and without FACTS devices under different loading conditions. Generator limits are ignored, and a typical PQ model is used for the loads. Voltage stability studies are performed by starting from an initial stable operating point and increasing the loads by a factor $\lambda$ until the singular point of the power flow linearization is reached. The loads in this case are defined as

$$\begin{aligned} P_L &= \lambda P_0 \\ Q_L &= \lambda Q_0 \end{aligned} \tag{5.1}$$

where $P_0$ and $Q_0$ are the active and reactive base loads, whereas $P_L$ and $Q_L$ are the active and reactive loads at a bus $L$ for the current operating point as defined by $\lambda$.

As the power flow solutions trajectory is traced for a load increase, the stable and unstable solutions come closer until they merge at the bifurcation point, as explained in chapter 2. The shape of this trajectory, known as the voltage profile or "nose" curve, is quadratic near the bifurcation or maximum loading point, as the bifurcation

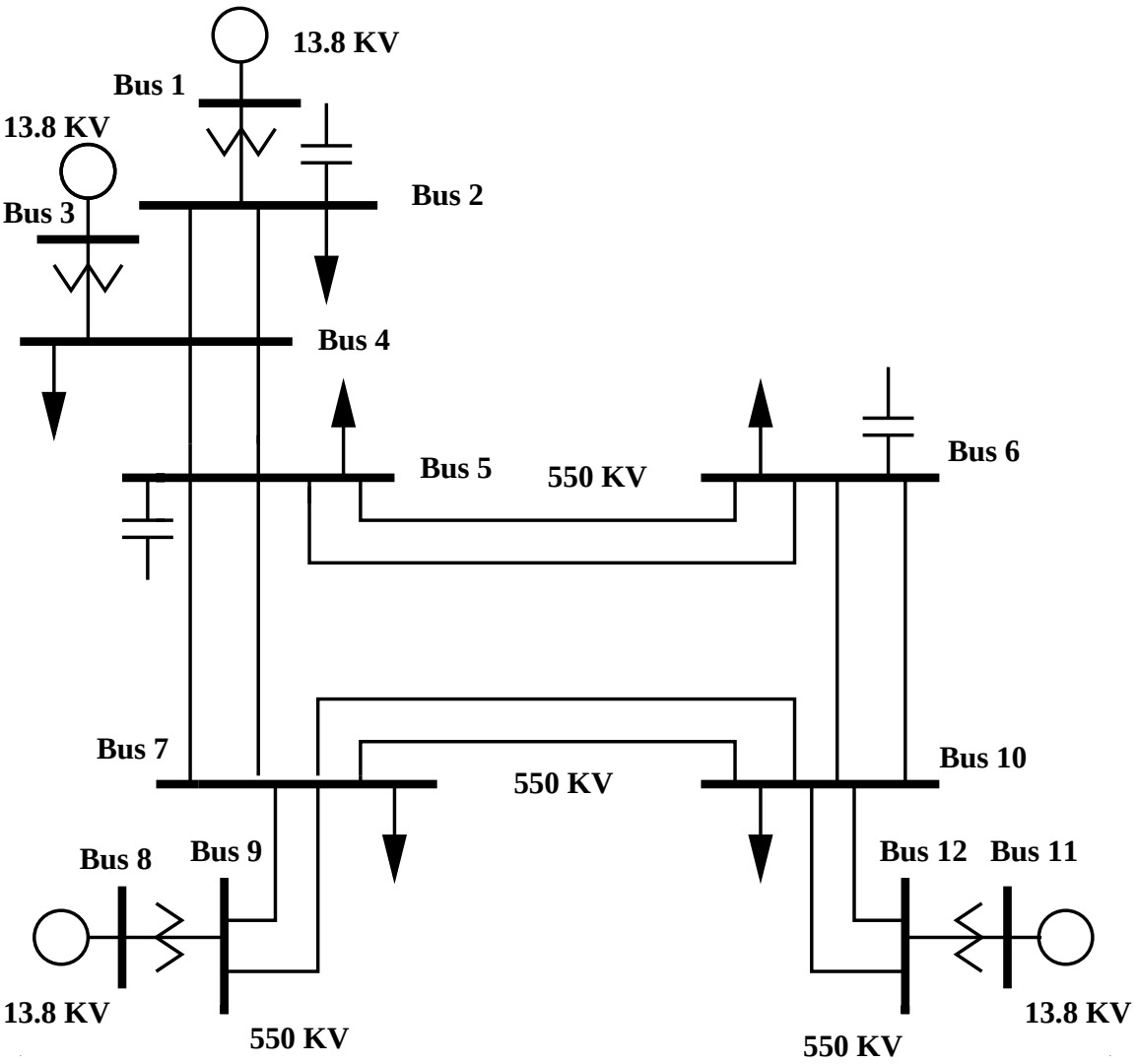


Figure 5.1: *12 bus test system.*

is generically a saddle-node. At the bifurcation point the right and left "zero" eigenvectors can be used to identify the bus(es) most prone to instability and the state variables which affect the system the most [10, 6, 19]. This information is used here for the system without FACTS devices, in order to find the optimal location and type of FACTS device to be placed within the system [46], as explained below.

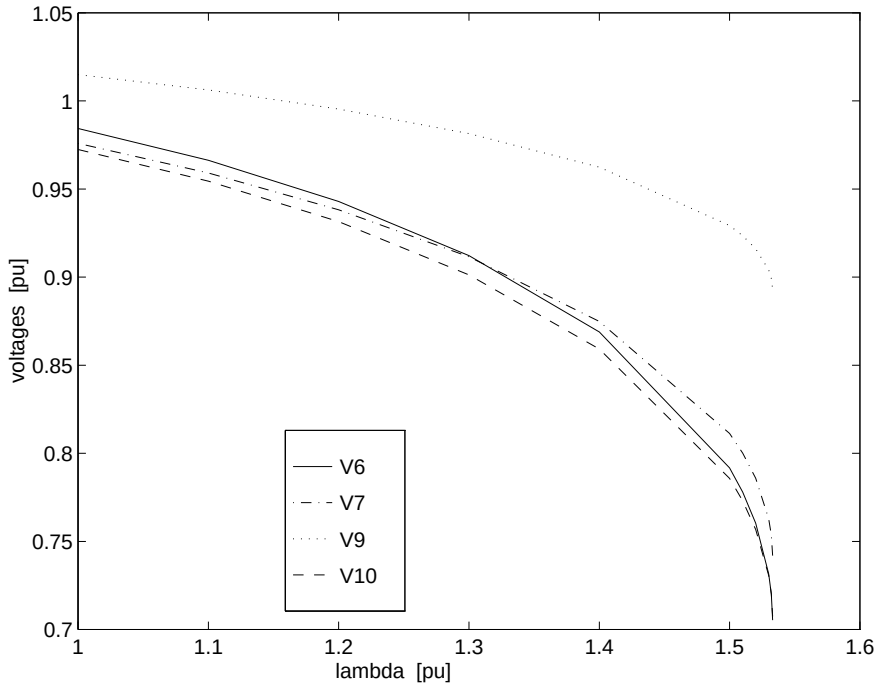


Figure 5.2: *Voltage profiles for the test system without FACTS* ($\lambda_{bif} = 1.533$).

The voltage profiles for chosen buses are presented in Figure 5.2 assuming a uniform load increase at all buses for P and Q. Voltage $V_i$ is the voltage at bus $i$, and $\lambda$ is the load increase parameter. At the bifurcation point, which corresponds to the maximum parameter value $\lambda_0 \approx 1.53$ in Figure 5.2, the voltage collapses. Using eigenvector analysis at the bifurcation point, the three most sensitive buses in terms of reactive power were identified as buses 6, 5, and 10, in that order. This result is consistent with the typical approach of voltage sensitivity factors [47, 48], i.e., $\Delta V/\Delta Q$, which yields the same results in this case. Based on these results, the optimal location of the SVC was chosen to be bus 6. In order to compare the effects of placing a SVC at various locations, another location was considered at bus 10.

In [49] the authors use a similar approach based on modal analysis to determine the optimal location of an SVC. It is shown in the paper that for a real system the voltage itself is a poor indicator of proximity to voltage collapse conditions, particularly when generator limits are considered. The sugested methodology is to use a continuation power flow together with eigenvector analysis.

For the test system, the left "zero" eigenvector indicates that the most sensitive bus, in terms of active power is bus 7. Therefore, a TCSC is placed on the most heavily loaded line, i.e., line 5-7; first at bus 7 and then at bus 5. In order to evaluate the effect of various locations of the TCSC, two other lines were considered, namely, line 7-10 and line 5-6.

## 5.2 Design of FACTS

### 5.2.1 SVC

After the optimal location of the SVC was determined to be at bus 6, the ratings of the SVC have to be chosen. It is to be expected that by introducing a SVC at that location, the voltage profiles will be flatter and the loadability margin of the system will increase. Assuming a typical control range for the voltage at that bus, i.e., $\pm$ 5 %, one can treat that bus as a PV bus with the voltage fixed at 0.95 p.u. This means placing a reactive power source, i.e., a synchronous compensator, at that bus. Considering that the SVC has to control the voltage at a loading level where the system without the SVC collapses, the required reactive power injection at that bus is found from the power flow. This is the maximum capacitive rating of the SVC. From Equation (3.15), the capacitive reactance of the SVC is

$$X_C\ [pu] = \frac{0.95^2}{Q_{MAX_C}\ [pu]} \tag{5.2}$$

If the inductive power rating of the SVC is considered equal to the capacitive rating at 1.05 p.u. bus voltage, then the inductive reactance $X_L$ of the SVC is 55 % of the capacitive reactance $X_C$ as shown in Equation 3.17. Considering equal current rating at the voltage range limits, a similar value of the inductive reactance is determined (Equation 3.18).

Another way of determining the inductive rating of the SVC is to solve the power flow at "minimum" load, with the SVC bus voltage fixed at 1.05 p.u. The reactive

power injection at that bus is the maximum inductive power of the SVC at the specified voltage. The minimum load is system dependent and has to be defined from historical data for that system. For the test system considered, the minimum load is assumed to be zero; this leads to a value of the SVC inductive reactance $X_L = 0.6X_C$. The choice of SVC parameters is consistent with existent devices, such as Hydro-Quebec's Nemiskau FC-TCR SVC [33]. The slope of the control characteristic is chosen to be 5 % with respect to the SVC base.

The load is increased from the base case to the bifurcation point causing a drop in bus voltages; therefore, the capacitive range of the SVC is used to provide reactive support to the system. Zero reactive power is provided at $\alpha = 112°$, where $X_V = X_C$. A 175° value of the maximum firing angle was chosen to avoid numerical problems caused by the 180° value. At the maximum capacitive limit, the SVC is transformed into a fixed reactance $X_C$.

### 5.2.2 TCSC

A chosen ratio $r_x = 10$, where $r_x = X_C/X_L$, determines the steady-state resonant point of the TCSC at $\alpha_{res} = 143°$. This is a typical value for $r_x$ [8]; other values of $r_x$ will shift the TCSC equivalent reactance characteristic to the right or to the left but the shape of the characteristic remains the same.

The TCSC equivalent reactance $X_e$ is controlled in the capacitive region between the minimum value $X_C$ and the maximum value, reached at 100 % line compensation. For the given value of the line impedance, the maximum (100 % compensation) value of the equivalent reactance is chosen to be $X_{e_{MAX}} = X_{LINE} = 3X_C$. This value is chosen based on the TCSC equivalent reactance characteristic, presented in Figure 5.3, such that $\alpha_m$ provides a suficiently large margin to resonance and acceptable harmonic content, even at high compensation levels. The minimum firing angle is then $\alpha_m = 148°$, and the maximum limit of the firing angle is chosen at $\alpha_M = 175°$, where the equivalent reactance is practically $X_C$, with a suficient margin to avoid numerical problems at $\alpha \approx 180°$. For each new location, the TCSC was redesigned such that it can be controlled from minimum to 100 % line compensation.

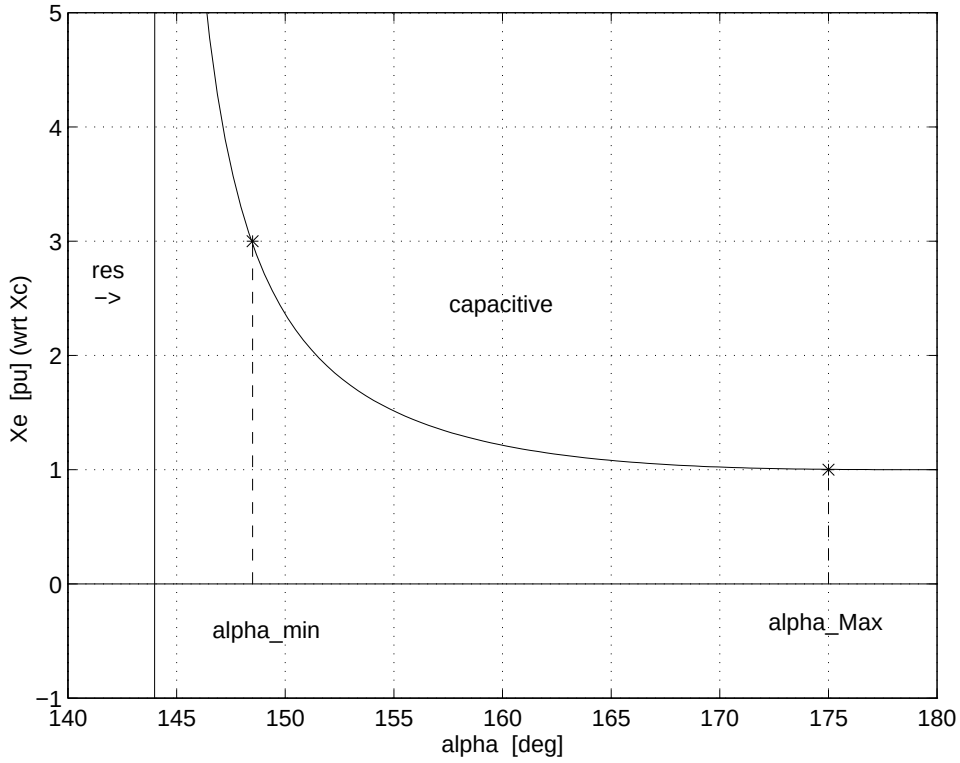


Figure 5.3: *TCSC equivalent reactance and firing angle limits.*

## 5.3 Example

### 5.3.1 SVC

The voltage profiles for the sytem with the SVC at bus 6 are shown in Figure 5.4. As expected, the bifurcation for the system with the SVC placed at bus 6 occurs at a higher load value, i.e., $\lambda_0 \approx 1.63$ (6.5 % larger than for the system without the SVC). Also, the voltage profiles are much flatter within the control limits of the SVC, which are reached by design at approximately the previous bifurcating value $\lambda \approx 1.53$.

The nose curves for the system with the same SVC located now at bus 10 are shown in Figure 5.5. The controlled range of the voltages is considerably less than for the SVC placed at bus 6. Furthermore, the bifurcation occurs at a lower load value of $\lambda_0 \approx 1.61$ (only 5.2 % larger than for the system without the SVC).

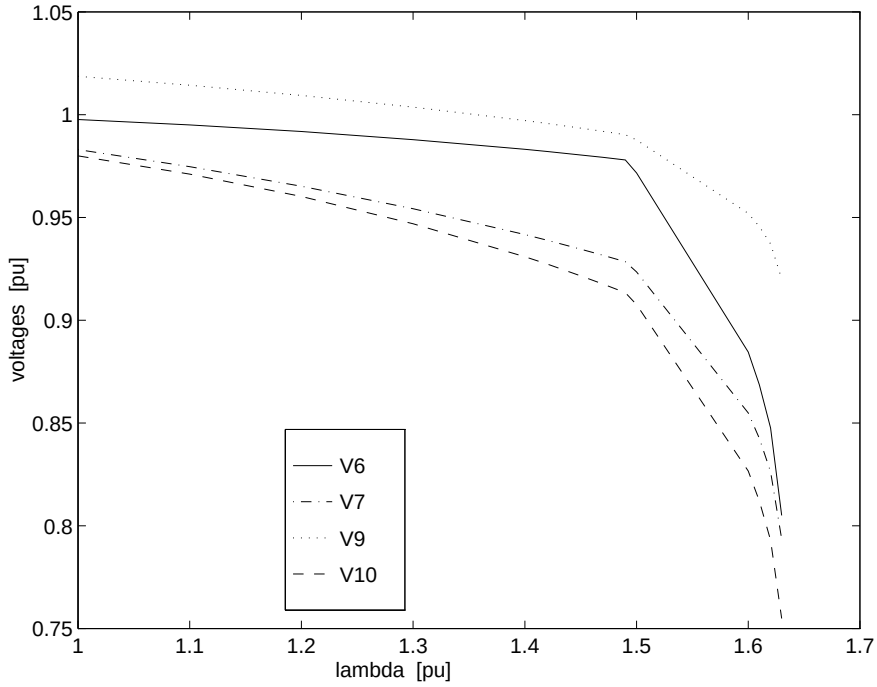


Figure 5.4: *Voltage profiles for the test system with the SVC at bus 6 ($\lambda_{bif} = 1.633$).*

In order to evaluate the performance of the system with the SVC in place, the following performance measure $f_p$, is proposed based on the loadability margin

$$f_p = \frac{\Delta\lambda \; MW_{init}}{Q_{SVC}} \tag{5.3}$$

where $MW_{init}$ is the total active load at the initial operating point, $Q_{SVC}$ is the SVC rating, and $\Delta\lambda$ is the difference between the values of $\lambda$ at the bifurcation for the system with and without the SVC. This performance measure can be changed to reflect the desired control voltage range, by defining $\Delta\lambda$ as the difference between the values of $\lambda$ for the system with and without the SVC, at a voltage value of 0.95 p.u. limit. Using either of these performance indices to evaluate the performance of the SVC within the system, it was determined that placing the SVC at bus 6 is the most cost effective for the test system.

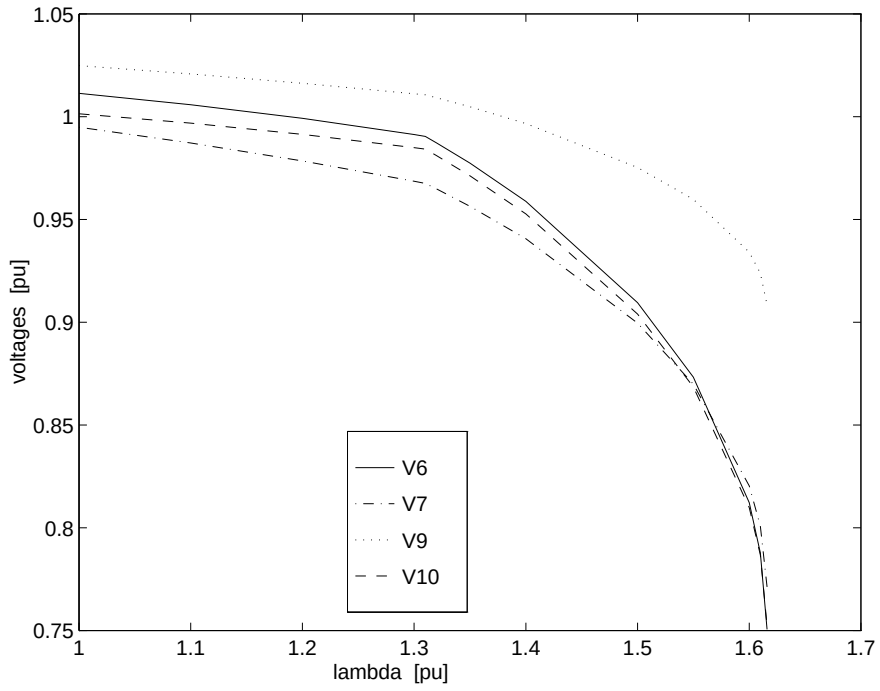


Figure 5.5: *Voltage profiles for the test system with the SVC at bus 10 ($\lambda_{bif} = 1.616$).*

### 5.3.2 TCSC

The voltage profiles for a TCSC placed on line 5-7 at bus 5 are shown in Figure 5.6. The bifurcation in this case occurs at $\lambda \approx 1.62$, almost at the same point as for the SVC located at bus 6; however, the voltage profiles are not as flat as in the SVC case. Placing the TCSC at bus 7 yields practically the same bifurcation point. Locating the TCSC in the less heavily loded line 5-6 produces a lower value of $\lambda_0 \approx 1.53$; a TCSC in line 7-10 gives $\lambda_0 \approx 1.55$ (Figure 5.7).

Using fixed power control with the TCSC located at bus 5, on line 5-7 with the power set at the same level as given by the 70 % compensation at the base load, the same bifurcation point is reached; however, the voltages drop faster within the controlled region as shown in Figure 5.8. This control strategy is more attractive when a specified corridor is to be used for a certain amount of power. In the case of fixed impedance control, 70 % compensation means a 333 % increase in the maximum power that could be transfered through the line.

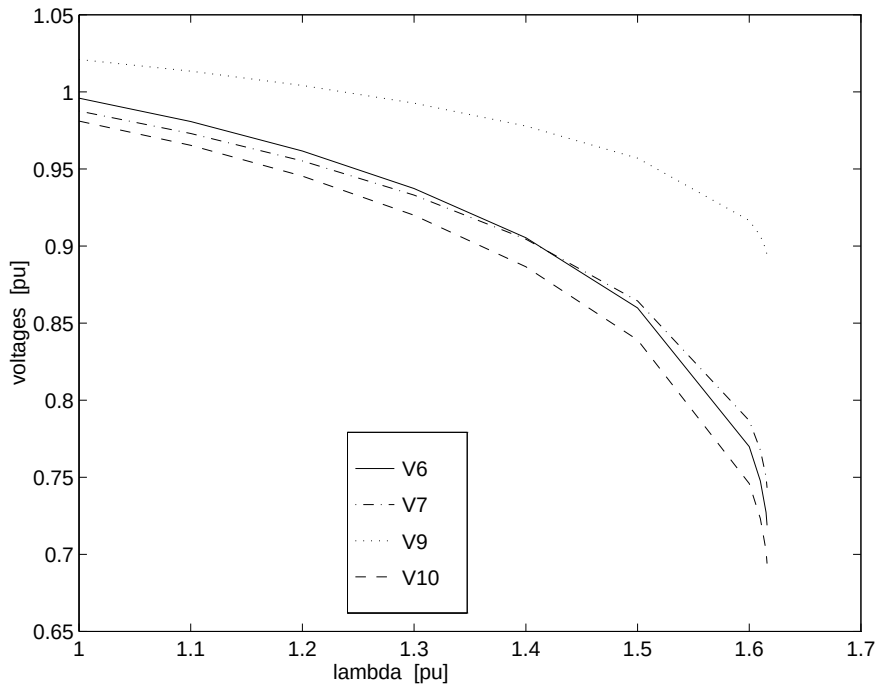


Figure 5.6: *Voltage profiles for the test system with 70 % TCSC compensation in line 5-7, at bus 5 ($\lambda_{bif} = 1.616$).*

In order to obtain the power set point, an initial analysis has to be performed with different compensation and loading levels. The power flow through the line with a fixed reactance control provides valid set points for the constant power control. Constant current control yielded almost identical results as the constant power case. The power flow results for the test system with the TCSC placed at bus 5, on line 5-7 are summarized in Table 5.1, where the last entry at each compensation level corresponds to the bifurcation point. For each compensation level the system was loaded from the initial point ($\lambda = 0.8$) to the maximum loadability point.

These preliminary studies are necessary in order to get the range of controllable set points, i.e., active power, line current and transmission angle. The transmission angle varies with the loading level between 7° and 14° for the noncompensated line, whereas for the 90 % compensated line it varies between 1° and 2°. Notice that the power flow through the line increases with the compensation and the loading level. However, the increase in the TCSC power is not proportional to the increase in the compensation

| $\lambda$ | 40 % | 70 % | 90 % | 95 % | 100 % |
|---|---|---|---|---|---|
| | $\mathbf{P_{5-7}}$ | $\mathbf{P_{5-7}}$ | $\mathbf{P_{5-7}}$ | $\mathbf{P_{5-7}}$ | $\mathbf{P_{5-7}}$ |
| 0.8 | 27.8 | 30.2 | 32.0 | 32.5 | 33.1 |
| 0.9 | 29.6 | 32.2 | 34.2 | 34.7 | 35.2 |
| 1.0 | 31.5 | 34.2 | 36.3 | 36.8 | 37.4 |
| 1.1 | 33.3 | 36.2 | 38.4 | 39.0 | 39.6 |
| 1.2 | 35.2 | 38.2 | 40.5 | 41.2 | 41.8 |
| 1.3 | 37.1 | 40.2 | 42.7 | 43.3 | 44.0 |
| 1.4 | 39.0 | 42.3 | 44.8 | 45.5 | 46.2 |
| 1.5 | | 44.4 | 47.0 | 47.7 | 48.4 |
| 1.6 | | 46.6 | 49.2 | 49.9 | 50.7 |
| 1.616 | | 47.0 | 49.6 | 50.3 | 51.1 |
| 1.641 | | | 50.3 | 50.9 | 51.7 |
| 1.646 | | | | 51.1 | 51.8 |
| 1.652 | | | | | 52.0 |

Table 5.1: Power flow in p.u. through line 5-7 at various compensation and load levels.

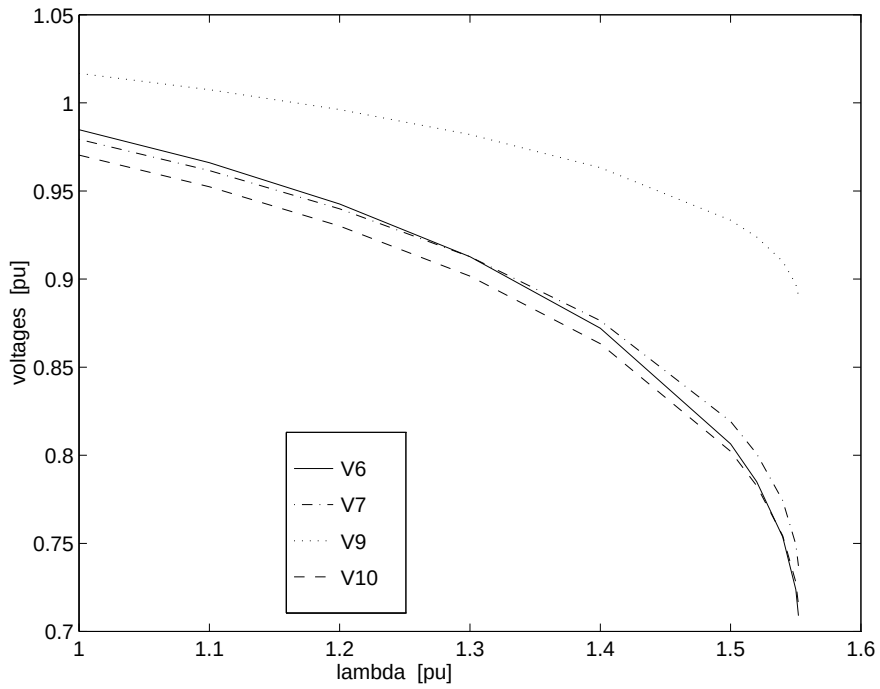


Figure 5.7: *Voltage profiles for the test system with 70 % TCSC compensation in line 7-10, at bus 7 ($\lambda_{bif} = 1.552$).*

level, as it would be expected when assuming that the line end voltages and angles are kept constant. For example, if the initial power flow through the noncompensated line is $P_{5\_7} = 28.34$ *p.u.* at the base load, from Table 5.1 it can be seen that at 100 % compensation level the power flow through the line increases only by about 32 %. This is due to the fact that the TCSC injects reactive power into the system, changing the line end voltages in magnitude and angle. The power flow through the line is system dependent and can only be determined from preliminary power flow studies. The approximate formula of Equation (3.22) yields eroneous results in the case of high compensation levels (e.g., at 90 % compensation the error margin is 18 %).

The fixed transmission angle control provides the maximum loadability margin if it is set at a low value. For example, $\delta_{5\_7} = 2.41°$ yields a bifurcation point at $\lambda_0 \approx 1.64$ (Figure 5.9).

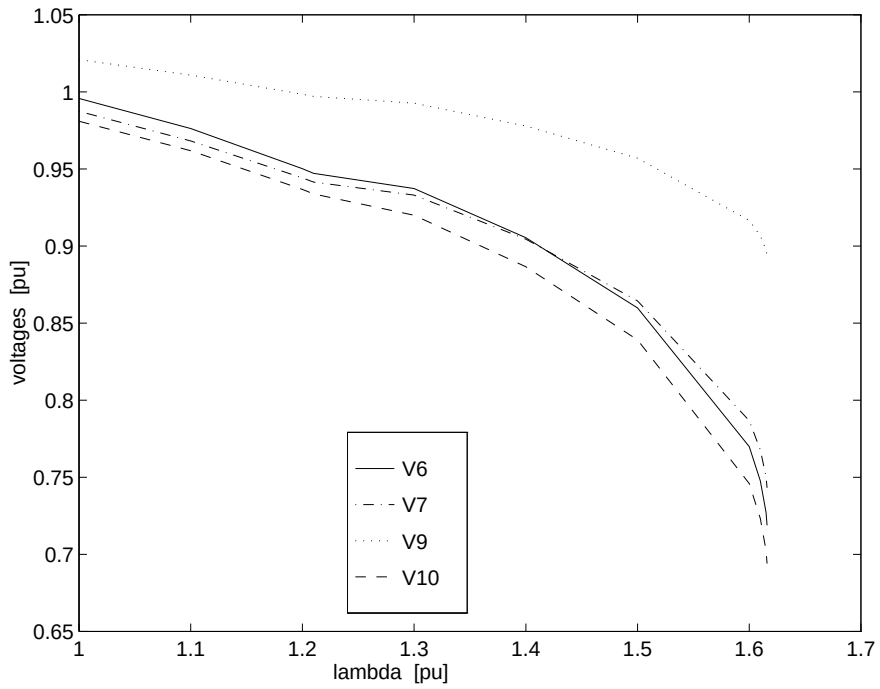


Figure 5.8: *Voltage profiles for the test system with fixed power TCSC control in line 5-7, at bus 5 ($\lambda_{bif} = 1.616$).*

In order to increase the loadability margin of the system another control strategy is considered. The TCSC is operated initially in the typical constant reactance control, at 70 % compensation level. As the system approaches the bifurcation point ($\lambda_0 \approx 1.61$ for this control mode) the control is switched to 95 % compensation level. This control strategy provides the largest loadability margin with $\lambda_0 \approx 1.646$ (Figure 5.10). The jump in the system trajectories is due to the control mode switching; it is assumed here that the system reaches another steady-state stable operating point. The system trajectories are switched from one manifold to another, corresponding to the two different control modes. Similar results were obtained when the control is switched to constant transmission angle, constant power or constant current. From these different strategies, the constant transmission angle provided the best results. However, all these control strategies required preliminary studies in order to get valid set points and initial guesses at the switching point.

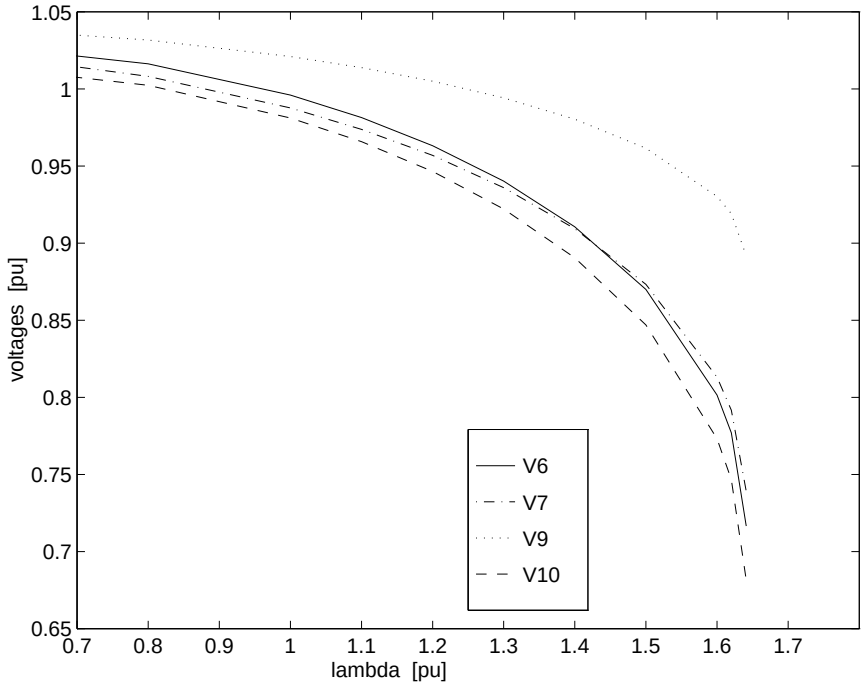


Figure 5.9: *Voltage profiles for the test system with fixed transmission angle control for the TCSC in line 5-7, at bus 5* ($\lambda_{bif} = 1.641$).

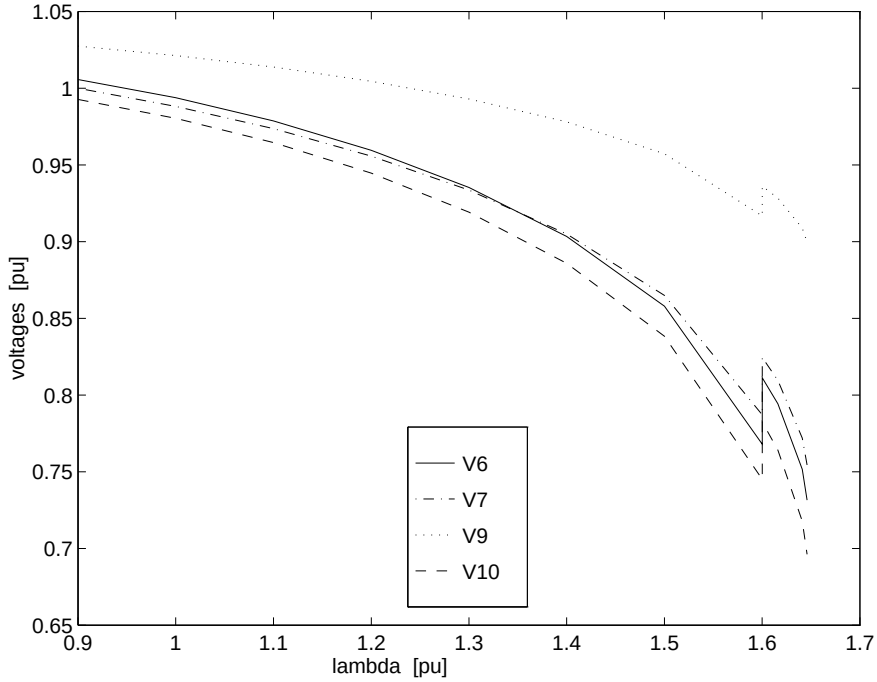


Figure 5.10: *Voltage profiles for the test system with 70 % and then 95 % line compensation for the TCSC in line 5-7, at bus 5* ($\lambda_{bif} = 1.646$).

# Chapter 6

# System studies

## 6.1 Software and System

The software that was used to analyse the 173 bus ac/dc system is PFLOW [17, 6, 13], and it was briefly described in Chapter 4. This program was enhanced by including SVCs and TCSCs using the models derived in Chapter 3, and the methodology presented in Chapter 4. The program is capable of handling any size ac/dc/FACTS systems, limited only by the available memory and swap space.

Figure 6.1 shows the one-line diagram corresponding to the 173 bus ac/dc system used in this thesis. This system is a simplified version of a real bus network, with ac transmission voltage levels of 500 kV, 345 kV and 230 kV. Both rectifier stations are weakly coupled through a long 500 kV transmission system, whereas the inverter ends are tightly coupled through a 500 kV–345 kV–230 kV ac network. The dc link on the left of Figure 6.1 is a 12 pulse bipolar HVDC system with a $\pm$500 kV dc voltage level and 3000 MW capacity; the second HVDC system is also a 12 pulse bipolar dc link designed for $\pm$500 kV and 2000 MW nominal levels. The ac system has 29 generators, 203 transmission lines and transformers, and 52 series capacitors [13].

Typical V and Q limits are included, as well as tap limits for the regulator transformers. In all cases, HVDC control switching and limits were considered; however, VDCOL was not included in the analyses. For all bifurcation analyses, constant load power at all buses was assumed to increase keeping the initial power factor unchanged. Also, all generators were given a participation factor according to their power capac-

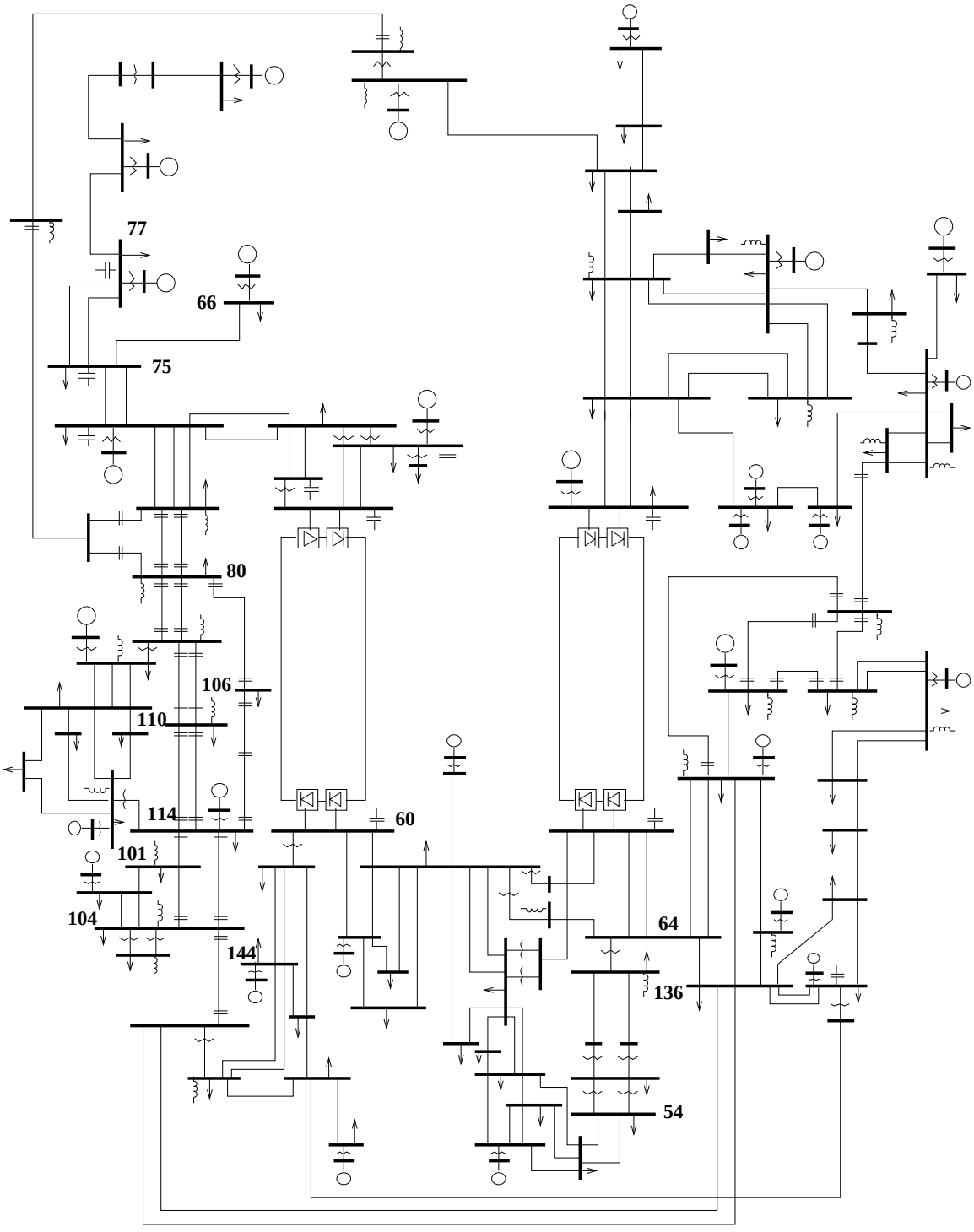


Figure 6.1: *173 bus ac/dc system.*

ity so that generation was evenly distributed across the networks (distributed slack bus) [13].

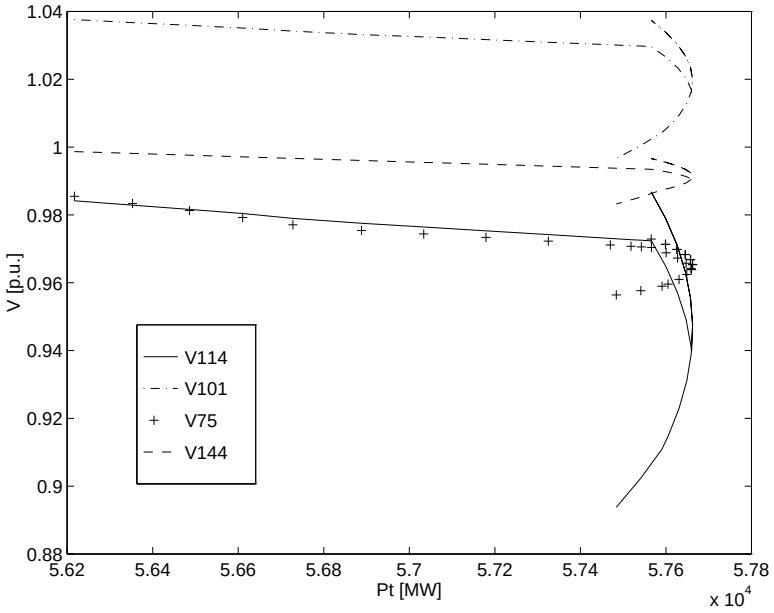


Figure 6.2: *Voltage profiles for 173 bus ac/dc system, without FACTS.*

## 6.2 Results

The voltage profiles at chosen buses are shown in Figure 6.2. These are the 4 voltages that change the most with respect to the loading of the system. The total active load for the base case is $P_{total} = 56,216.91$ MW. The active and reactive load is increased discretely, according to the load model. The PV diagrams are used to show the voltage profiles versus the total active load, since active power is the most "useful" component of the load, and can be assigned a monetary value. Notice that the voltage profiles in the PV diagram (Figure 6.2) are quite flat, which means that there is significant voltage suport in the system. The bifurcation point is reached at high values of the voltages, close to 1.0 p.u., which indicates that the voltages itself is a poor indicator of voltage collapse. At the bifurcation point, which is reached at $P^{bif}_{total} = 57,656.06$ MW, the stable and unstable manifolds meet with a maximum Q-limit manifold [10]. This is due to several generators hitting Q limits. The continuation method traces

the stable manifold of the system, goes around the bifurcation point and traces part of the other manifold.

Eigenvector analysis applied at the bifurcation point provided the 2 buses that lack voltage support the most as buses 114 and 101. Bus 75 has a lower priority and it is used to show the importance of SVC location. The optimal choice for the SVC location is bus 114.

To design the SVC, bus 114 was changed into a PV bus with the voltage fixed at 0.98 p.u. The solution to the power flow at the loading level where the original system bifurcates, i.e., $P_{total}^{bif} = 57,656.06$ MW, indicates that the required reactive power injection is about 200 Mvar. The inductive rating of the SVC is assumed to be equal to its capacitive rating; therefore, $Q_{SVC} = \pm 200$ Mvar. The slope of the SVC is 2 %. The rated voltage at bus 114 is 500 KV, and the SVC is connected to that bus through a step-down transformer. The low voltage of the transformer is chosen as 26 KV and its equivalent reactance as 10 % with respect to its own base, which is the same as the SVC base. These are typical values for a SVC and the associated step-down transformer [33].

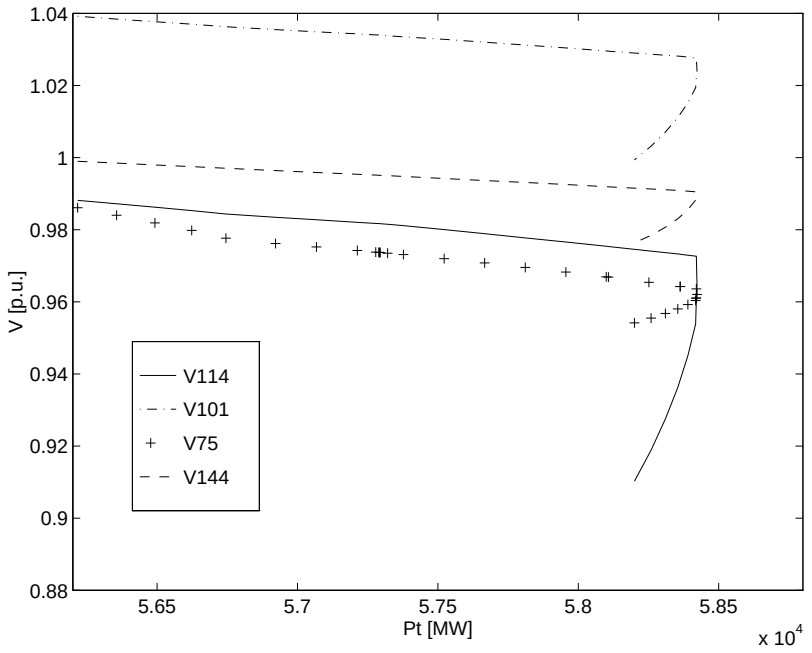


Figure 6.3: *Voltage profiles for 173 bus ac/dc system with* $Q_{SVC} = \pm 200$ *Mvar, slope=2 %,* $V_{REF} = 1.0$*, at bus 114.*

The bifurcation diagram for the SVC placed at bus 114 is presented in Figure 6.3. The bifurcation occurs at $P_{total}^{bif} = 58,431.86$ MW, which is 3.94 % more than the base load. The performance factor is $f_P = 11.075$. The system with the SVC placed at bus 114 is capable of delivering 2,214.95 MW of additional power for a $\pm$200Mvar rating of the SVC. An estimate of the monetary value may be done by assuming that one makes use of 10 % of the additional margin for 1 year. Considering further a cost of 0.02 USD /KWh to produce the energy and 10 % profit, a profit of approximately 3.9 milion USD /year can be estimated for a $\pm$200 Mvar SVC investment.

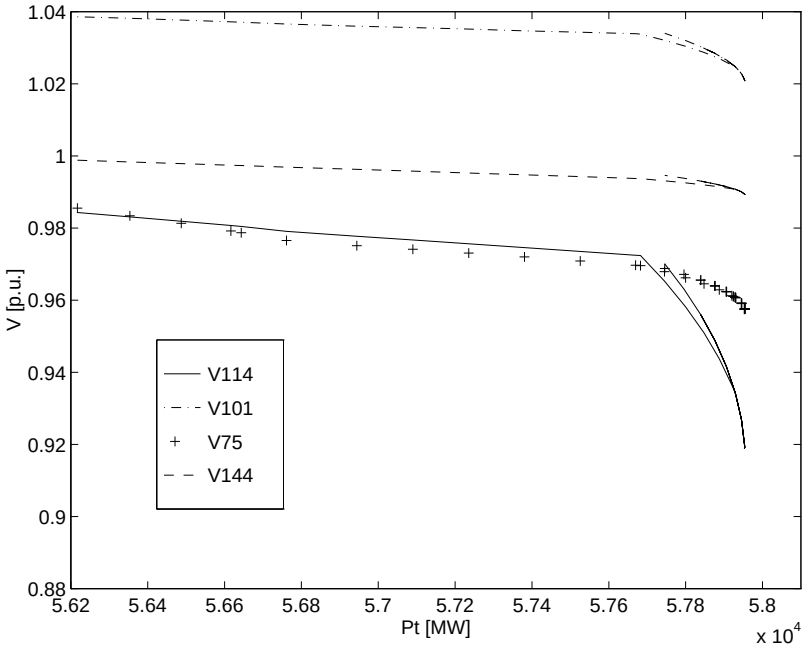


Figure 6.4: *Voltage profiles for 173 bus ac/dc system with* $Q_{SVC} = \pm 200$ *Mvar, slope=2 %,* $V_{REF} = 1.04$*, at bus 101.*

Figure 6.4 shows the voltage profiles for the same SVC placed at bus 101. The maximum load that can be delivered in this case is $P_{total}^{bif} = 57,956.63$ MW, which is 0.85 % less than for the same SVC placed at bus 114. Notice that the voltage at bus 101 is very high as compared to the other voltages; therefore, the reference voltage for the SVC is set at 1.04 p.u.

Figure 6.5 presents the voltage profiles for the same SVC placed at bus 75. The maximum loadability point is reached at $P_{total}^{bif} = 57,802.23$ MW, which is 1.12 % less

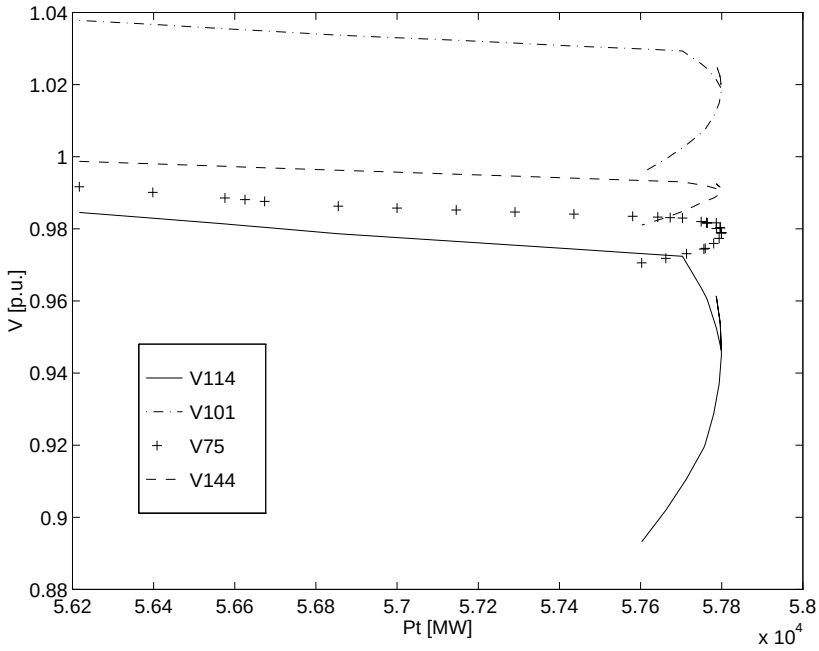


Figure 6.5: *Voltage profiles for 173 bus ac/dc system with* $Q_{SVC} = \pm 200$ *Mvar, slope=2 %,* $V_{REF} = 1.0$*, at bus 75.*

than for the SVC placed at bus 114. The results presented in Figures 6.3, 6.4, and 6.5 show the effect of SVC location on the loadability margin of the system and validate the information obtained from eigenvector analysis.

Bifurcation analysis is performed on the system with the SVC placed at bus 114. The analysis indicates that voltage support is again mostly needed at bus 114. The same design method as previously shown is used and the amount of additional reactive support is about 100 Mvar; therefore, a SVC of ratings $Q_{SVC} = \pm 300$ Mvar is placed at bus 114 replacing the $\pm 200$ Mvar SVC. The same transformer is used with a new rating equal to the new SVC rating. The voltage profiles are shown in Figure 6.6. The maximum load is now $P_{total}^{bif} = 58,856.29$ MW, or 0.72 % more than for the $\pm 200$ Mvar SVC at the same bus. It can be concluded that this improvement is marginal with respect to the base case, where the $\pm 200$ Mvar SVC was placed at bus 114. This is better revealed by using the proposed performance factor. For the $\pm 200$ Mvar SVC placed at bus 114 the performance factor is $f_{P1} = 11.075$, whereas for the $\pm 300$ Mvar SVC placed at the same bus the new performance factor is $f_{P2} = 8.798$, which is considerably lower. In other words placing the $\pm 200$ Mvar SVC at bus 114 is more

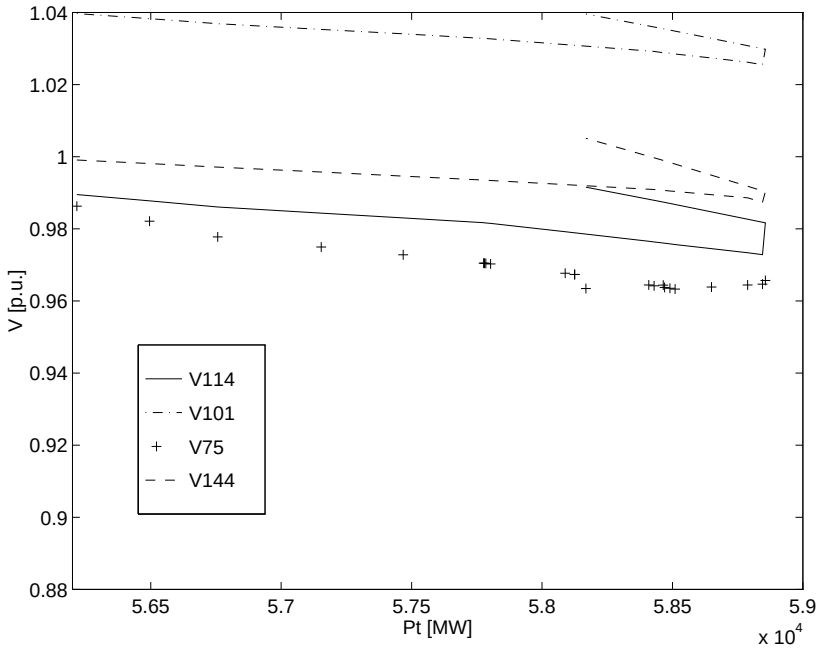


Figure 6.6: *Voltage profiles for 173 bus ac/dc system with* $Q_{SVC} = \pm 300$ *Mvar, slope=2 %,* $V_{REF} = 1.0$*, at bus 114.*

(cost) effective than placing an additional $\pm 100$ Mvar at that bus by rating the SVC at $\pm 300$ Mvar.

Another location is chosen at bus 60 for a second SVC rated at $\pm 100$ Mvar. This corresponds to the extra $\pm 100$ Mvar added to the SVC at bus 114. The voltage reference is set at 1.02 p.u. due to the initial voltage profile at bus 60. This is the inverter bus for one of the HVDC links and it was ranked lower than bus 114 or 101, by the eigenvector analysis. Figure 6.7 presents the results for this 2 SVC case. The maximum load is $P_{total}^{bif} = 58,437.47$ MW, or 0.01 % higher than for the $\pm 200$ Mvar SVC placed at bus 114. This result is once again consistent with eigenvector analysis.

Eigenvector analysis performed on the original system also indicates that there is a lack of active support at buses 65, 66, in that order, and 77, 75 with a lower priority. For the system configuration with fixed generation, power flow through lines 66-75 or 77-75 is fixed and cannot be affected by series compensation because there are no alternative routes for the power to flow (Figure 6.1). The next buses with lack of active support are buses 136, 54 and 114. The most heavily loaded lines are lines 114-

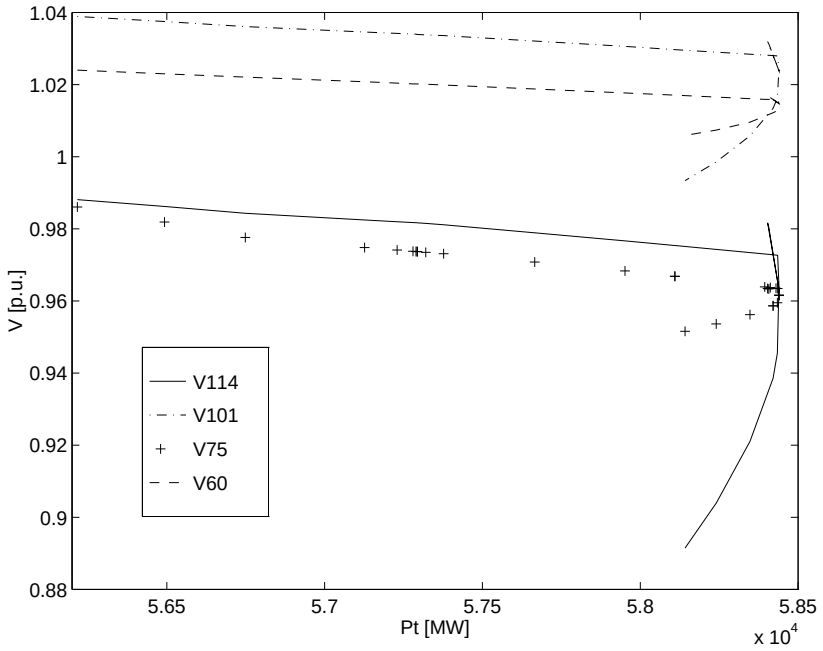


Figure 6.7: *Voltage profiles for 173 bus ac/dc system with* $Q_{SVC1} = \pm 200$ *Mvar, slope=2 %,* $V_{REF} = 1.0$*, at bus 114 and* $Q_{SVC2} = \pm 100$ *Mvar, slope=2 %,* $V_{REF} = 1.02$*, at bus 60.*

106, 114-110 (short) and 114-110 (long), in that order. All of these lines are already series compensated. Bus 114 is connected to bus 110 through 2 lines, a shortline and a long line. Figure 6.8 shows the voltage profiles for a TCSC placed on line 114-110 (short), at bus 114. The control is reactance control with 90 % compensation level (the base case had 52 % compensation on this line). The maximum load in this case is $P_{total}^{bif} = 58,744.42$ MW, or 4.5 % higher than the base case. Figure 6.9 shows the results for the same TCSC with power control fixed at the corresponding power flowing through the line at base loading and 90 % line compensation. The maximum load is $P_{total}^{bif} = 58,646.04$ MW, or 4.3 % higher than the base case. In Figure 6.10 the voltage profiles are presented for the same TCSC with current control set at the value of the current corresponding to base loading and 90 % line compensation. The maximum load is $P_{total}^{bif} = 58,555.53$ MW, or 4.16 % more than the base case. In Figure 6.11 the PV diagram is presented for constant transmission angle control, set at the angle corresponding to base loading and 90 % line compensation. The maximum power is in this case $P_{total}^{bif} = 58,605.00$ MW, or 4.25 % higher than the

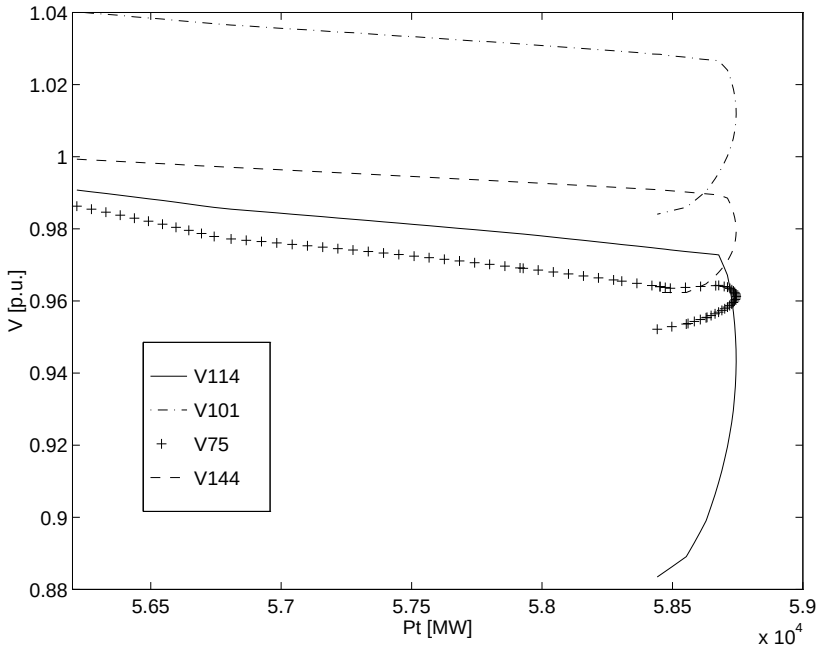


Figure 6.8: *Voltage profiles for 173 bus ac/dc system, TCSC on line 114-110 (short), 90 % compensation.*

base case. From the 4 control strategies presented, constant reactance, which is the typical control strategy, provided the maximum loadability margin.

Figure 6.12 presents the results for a TCSC placed on the line 114-110 (long), with constant reactance control, at 90 % compensation level. The original compensation was 66 %. The maximum load is $P_{total}^{bif} = 58,422.29$ MW, or 3.92 % increase. This is lower than the 4.5 % increase obtained for the short line, with the same compensation level.

In Figure 6.13 the voltage profiles for 2 TCSCs, placed on lines 114-110, are presented. The control is constant reactance at 90 % compensation level, for both lines. The maximum load in this case $P_{total}^{bif} = 58,990.65$ MW, or 4.93 % increase. Figure 6.14 shows the results for a TCSC placed on line 114-106 with constant reactance control at 90 % compensation level. The original compensation level is 74 %, which motivated the 90 % compensation level chosen for all cases. The maximum load in this case is $P_{total}^{bif} = 58,306.49$ MW, or 3.72 % increase.

Another location, with a lower priority in the eigenvector analysis, is chosen to

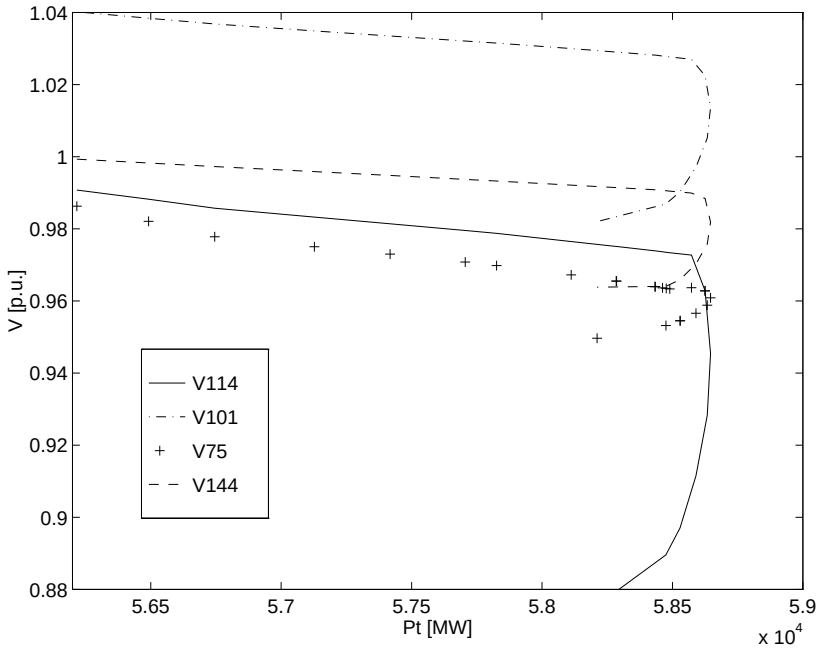


Figure 6.9: *Voltage profiles for 173 bus ac/dc system, TCSC on line 114-110 (short), power control.*

place a TCSC, namely, at bus 136, on line 136-64. The initial line was uncompensated. The control mode is reactance control at 90 % compensation level. The maximum load in this case is $P_{total}^{bif} = 57,708.90$ MW, or 2.65 % increase with respect to the base case. The voltage profiles for this case are presented in Figure 6.15. This example shows the effect of TCSC placement on the loadability margin of the system, validating the information provided by eigenvector analysis.

In conclusion, eigenvector analysis combined with the continuation power flow and FACTS design methodology, provided promising results for the 173 bus ac/dc system, which are consistent with the results obtained for the 12 bus test system. The effect of FACTS devices is to increase the loadability margin of the system, with SVCs giving flatter voltage profiles. The placement of FACTS using eigenvector analysis is certainly a usefull tool for maximizing the loadability margin in a system.

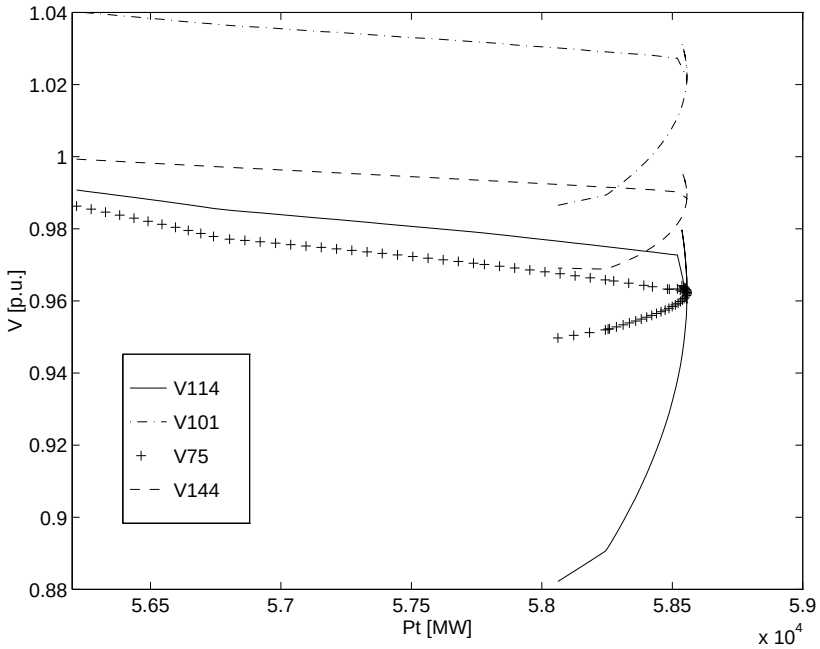


Figure 6.10: *Voltage profiles for 173 bus ac/dc system, TCSC on line 114-110 (short), current control.*

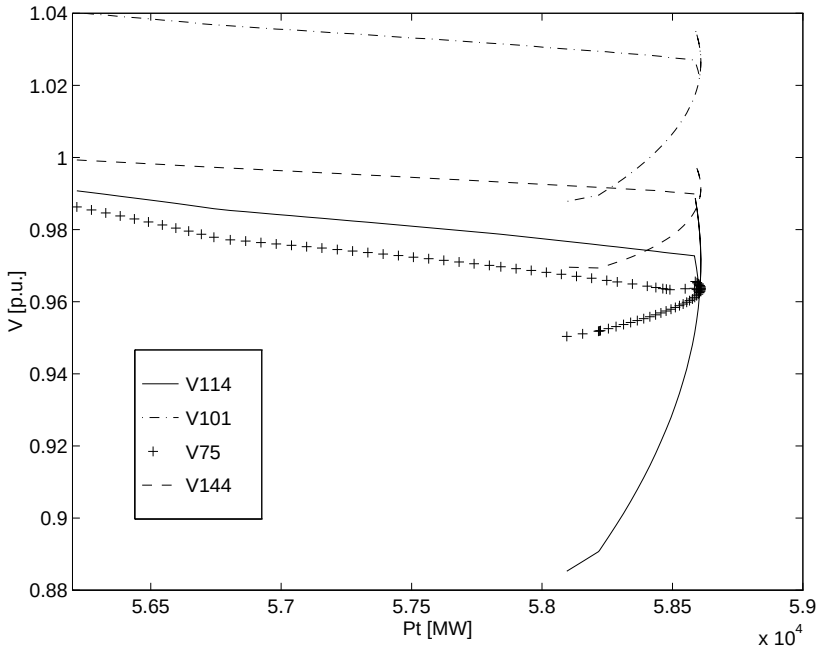


Figure 6.11: *Voltage profiles for 173 bus ac/dc system, TCSC on line 114-110 (short), transmission angle control.*

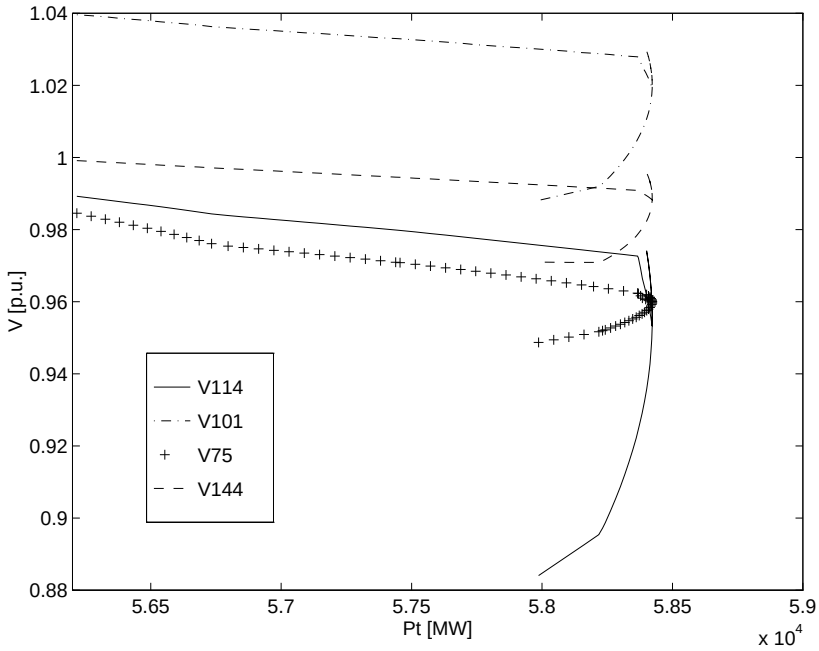


Figure 6.12: *Voltage profiles for 173 bus ac/dc system, TCSC on line 114-110 (long), 90 % compensation.*

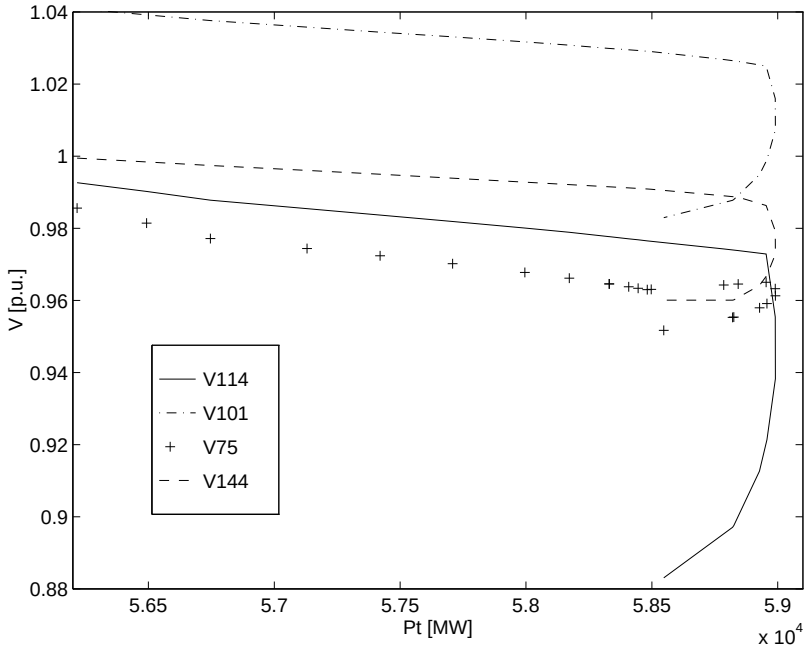


Figure 6.13: *Voltage profiles for 173 bus ac/dc system, TCSC1 on line 114-110 (long), 90 % compensation, TCSC2 on line 114-110 (short), 90 % compensation.*

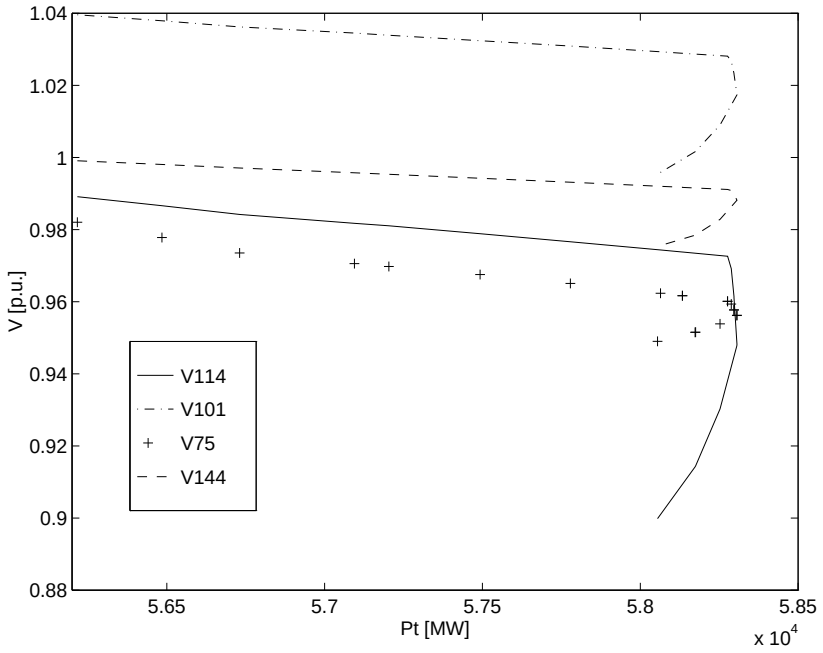


Figure 6.14: *Voltage profiles for 173 bus ac/dc system, TCSC on line 114-106, 90 % compensation.*

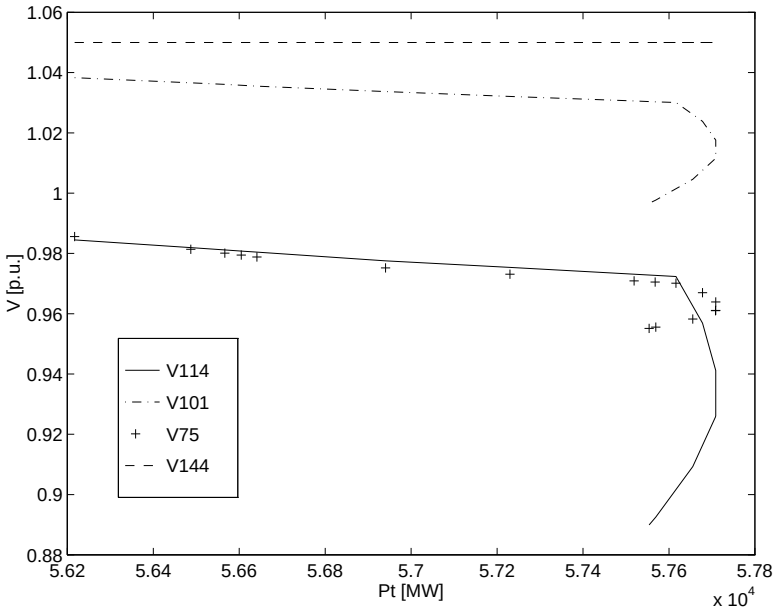


Figure 6.15: *Voltage profiles for 173 bus ac/dc system, TCSC on line 64-136, 90 % compensation.*

# Chapter 7

# Conclusions

Voltage collapse phenomena and FACTS devices are reviewed together with bifurcation theory. Steady-state models of an SVC and a TCSC are proposed and compared to dynamical models. Different control strategies and handling of limits are then discussed for each of these devices.

A methodology to implement these FACTS devices in a power flow is presented together with the continuation power flow, which is the chosen technique to investigate voltage instability in a power system. A method for placing and designing these devices, based on bifurcation analysis, is also discussed. The results of the studies performed on a 12 bus and then on a 173 bus ac/dc system are presented, and a performance measure is proposed to evaluate the effect of FACTS devices on the system.

The major contributions of this thesis can be summarized as follows:

1. Steady-state models of a SVC and a TCSC, including controls and limits, are proposed.
2. A methodology to implement these devices in a power flow is presented.
3. A method for placing and designing SVCs and TCSCs, within a system, such that its loadability margin is increased in a most efficient way is presented.
4. SVCs and TCSCs were implemented in PFLOW [6, 17], enhancing the capabilities of this software and allowing the methodology to be tested in large systems. A "WSCC type" format for SVCs and TCSCs is proposed, since currently there is no standard for SVC and TCSC power flow data.

5. A performance measure to evaluate the effect of FACTS on a power system is proposed and discussed for a 173 bus ac/dc system.

6. The models and the methodology are tested for a 12 bus and then for a realistic 173 bus ac/dc system with promising results.

Most of the ideas presented in this thesis have been summarized in [46].

Considering other FACTS devices such as the Static Compensator (STATCOM) or the Universal Power Flow Controller (UPFC) is worth further study. The implementation of these devices, with their controls and limits, in PFLOW would allow for the evaluation of the effect of different FACTS devices on a system, from an operational and planning perspective. The proposed performance measures can be extended to the new devices and if specific information for a system is made available, a monetary value can be derived.

Another idea which could be considered is the optimal design of a FACTS device, with generic controls, such that the loadability of the system is optimal [16].

# Appendix A

# SVC and TCSC data format

## A.1 SVC

The format used to input SVC data is a "WSCC type" format. It uses 80 characters per item, and the information regarding the type of data card, ownership, bus name(s) and KV is consistent with the WSCC format for branch data. The data card with an example for SVC data is presented in Table A.1.

| T | O | Name1 | KV1 | | Name2 | KV2 | $X_C$ | $X_L$ | $\alpha_m$ | $\alpha_M$ | $X_{sl}$ | MVA | $V_R$ | KVL | $X_{th}$ | $\alpha$ |
|---|---|---|---|---|---|---|---|---|---|---|---|---|---|---|---|---|
| FS | 1 | BUS_3 | 500 | | BUS_3 | 500 | .96 | .45 | 90 | 175 | 2 | 50 | 1.0 | 26.0 | 0.1 | |

Table A.1: SVC power flow data format.

A description of the meaning for each column of the card follows

**1** Card type (A1) $\rightarrow$ F for all FACTS cards.

**2** Sub-type (A1) $\rightarrow$ S for SVCs.

**3** Not used.

**4-6** Ownership code (I3) $\rightarrow$ may be used for losses summarry.

**7-18** Bus Name1 (A12) → alphanumeric in columns 7-14 and base KV1 in columns 15-18. Name of the system bus where the SVC is connected (directly or through a transformer).

**19** Not used.

**20-31** Bus Name2 (A12) → alphanumeric in columns 7-14 and KV2 in columns 15-18. Name of the system bus at which the SVC controls the voltage (can be different from Bus Name1).

**32-39** $X_C$ (F8.6) → p.u. reactance of SVC capacitor, with respect to the SVC base, i.e., MVA and KV1.

**40-47** $X_L$ (F8.6) → p.u. reactance of SVC inductor, with respect to the SVC base, i.e., MVA and KV1.

**48-50** $\alpha_{min}$ (I3) → minimum value allowed for the firing angle, in degrees (default 90°).

**51-53** $\alpha_{Max}$ (I3) → maximum value allowed for the firing angle, in degrees (default 180°).

**54-55** $X_{sl}$ (I2) → SVC control slope, in % with respect to the SVC base, i.e., MVA and KV1.

**56-59** MVA (F4.1) → SVC maximum rating in MVar (capacitive).

**60-63** $V_{REF}$ (F4.2) → p.u. value of the reference voltage in the control characteristic.

**64-67** KVL (F4.2) → low voltage of the step-down transformer, in KV.

**68-75** $X_{th}$ (F8.6) → p.u. value of the step-down transformer equivalent impedance, with respect to the SVC base, i.e., MVA and KV1.

**76-80** $\alpha$ (F5.1) → initial value of the firing angle, in degrees (blank if not known).

## A.2 TCSC

The data card for the TCSC uses the same "WSCC type" format. The data card with an example for TCSC data is presented in Table A.2.

| T | O | Name1 | KV1 | | Name2 | KV2 | $X_C$ | $X_L$ | $\alpha_m$ | $\alpha_M$ | ctrl | M | $MVA$ | $\alpha$ | M1 |
|---|---|---|---|---|---|---|---|---|---|---|---|---|---|---|---|
| FC | 1 | BUS_3A | 500 | | BUS_3 | 500 | .0075 | .00075 | 144 | 175 | 70 | X | | | 4. |

Table A.2: TCSC power flow data format.

A description of the meaning for each column of the card follows

**1** Card type (A1) → F for all FACTS cards.

**2** Sub-type (A1) → C for TCSCs.

**3** Not used.

**4-6** Ownership code (I3) → may be used for losses summary.

**7-18** Bus Name1 (A12) → alphanumeric in columns 7-14 and base KV1 in columns 15-18. Name of the system bus 1 where the TCSC is connected. Power flow is by convention from bus 1 to bus 2, if the direction of the power flow is opposite to this convention, the power through the TCSC has a negative sign. (To avoid this interchange Bus Name1 and Bus Name2).

**19** Not used.

**20-31** Bus Name2 (A12) → alphanumeric in columns 7-14 and KV2 in columns 15-18. Name of the system bus 2 where the TCSC is connected.

**32-39** $X_C$ (F8.6) → p.u. reactance of TCSC capacitor, with respect to the TCSC base, i.e., MVA and KV1.

**40-47** $X_L$ (F8.6) → p.u. reactance of TCSC inductor, with respect to the TCSC base, i.e., MVA and KV1.

**48-50** $\alpha_{min}$ (I3) → minimum value allowed for the firing angle, in degrees (default 90°).

**51-53** $\alpha_{Max}$ (I3) → maximum value allowed for the firing angle, in degrees (default 180°).

**54-61** ctrl (F8.3) → TCSC control value, in % if X mode, in MW if P mode, in KA if I mode and in degrees if D mode.

**62** M (A1) → control mode (character). X for constant reactance mode, P for constant power mode, I for constant current mode and D for constant transmission angle mode.

**63-66** MVA (F4.1) $\rightarrow$ TCSC maximum rating in MVA (equal to system MVA if not specified).

**67-71** $\alpha$ (F5.1) $\rightarrow$ initial value of the firing angle, in degrees (blank if not known).

**72-74** M1 (I3) $\rightarrow$ design value for the TCSC, defining the control range of the TCSC, i.e., $X_e = M1X_C = X_{line}$ at 100 % compensation and $X_e = X_c = X_{line}/M1$ at minimum compensation level. This information is needed in the X control mode, since the control value is specified in % of the line reactance. $M1$ is the ratio between the line reactance and the TCSC's capacitor reactance.

# Bibliography


[1] Carson W. Taylor,*Power System Voltage Stability*, McGraw-Hill, 1994.

[2] IEEE Committee Report, "Voltage Stability of Power Systems: Concepts, Analytical Tools, and Industry Experience," *IEEE/PES 90TH0358-2-PWR*, 1990.

[3] CIGRE WG 38.02 Task Force No.10 Report, "Modelling of Voltage Collapse Including Dynamic Phenomena," CIGRE technical report of task force 38-02-10, April 1993.

[4] IEEE Task Force on Terms & Definitions, "Proposed terms and definitions for power system stability," *IEEE Trans. Power Apparatus and Systems*, Vol. 101, No. 7, July 1982, pp. 1894-1898.

[5] Y. Mansour, editor, "Suggested techniques for voltage stability analysis," *technical report 93TH0620-5PWR, IEEE/PES* , 1993.

[6] C. A. Cañizares and F. L. Alvarado,"Point of Collapse and Continuation Methods for Large AC/DC Systems," *IEEE Trans. Power Systems*, Vol. 8, No. 1, February 1993,pp. 1-8.

[7] G.K. Morison and P. Kundur,"Voltage Stability Analysis Using Static and Dynamic Approaches," *IEEE Trans. Power Systems*, Vol. 8, No. 3, pp. 1159-1172.

[8] D. Marakutulam, editor, *Proc. FACTS Conference I—The Future in High-Voltage Transmission*, TR-100504, EPRI, March 1992.

[9] R. Seydel, *From Equilibrium to Chaos—Practical Bifurcation and Stability Analysis*, Elsevier Science, North-Holland, 1988.

[10] I. Dobson,"Observations on the geometry of saddle node bifurcations and voltage collapse in electrical power systems," *IEEE Transactions on Circuits and Systems – I*, Vol. 39, No. 3, March 1992, pp. 240- 243.

[11] I. Dobson and D. Chiang," Towards a theory of voltage collapse in electric power systems," *Systems Control Letters*, Vol.13, 1983, pp. 253-262.

[12] C. A. Cañizares, "Conditions for saddle-node bifurcations in AC/DC power Systems," *Int. J. of Electric Power & Energy Systems,"* Vol. 17, No. 1, February 1995, pp. 61-68.

[13] C. A. Cañizares, *Voltage Collapse and Transient Energy Function Analyses of AC/DC Systems*, PhD thesis, University of Wisconsin-Madison, 1991.

[14] B. Gao, G.K. Morison and P. Kundur,"Voltage Stability evaluation using modal analysis," *IEEE Trans. Power Systems*, Vol.7, No.4, pp. 1529-1542.

[15] C. A. Cañizares and S. Hranilovic, "Transcritical and Hopf Bifurcations in AC/DC Systems," *Proc. Bulk Power System Voltage Phenomena III – Voltage Stability and Security*, ECC Inc. Fairfax, VA, August 1994.

[16] C.A. Cañizares, "Calculating Optimal System Parameters to Maximize the Distance to Saddle-node Bifurcations," *Technical Report no.95-07*, University of Waterloo, July 5, 1995.

[17] C. A. Cañizares, F. L. Alvarado, C. L. DeMarco, I. Dobson and W. F. Long, "Point of Collapse Methods Applied to AC/DC Power Systems," *IEEE Trans. Power Systems*, Vol. 7, No. 2, May 1992, pp. 673-683.

[18] J. Arrillaga and C.P. Arnold, *Computer Analysis of Power Systems*, John Wiley, 1990.

[19] C. A. Cañizares, "On Bifurcations, Voltage Collapse and Load Modeling," IEEE/PES 94 SM 512-4 PWRS, San Francisco, CA, July 1994.

[20] W. Rudin, *Principles of Mathematical Analysis*, Mc Graw-Hill, USA, 1976.

[21] J. Guckenheimer and P. Holmes, *Nonlinear Oscillations, Dynamical Systems, and Bifurcations of Vector Fields*, Springer-Verlag, New York, USA, 1986.

[22] P.A. Löf, T. Smed, G. Anderson and D.J. Hill, "Fast Calculation of a Voltage Stability Index," *Trans. Power Systems*, Vol. 7, No.1, February 1992, pp. 54-64.

[23] J. Arrillaga, *High Voltage Direct Current Transmission*, Peter Peregrinus, London, UK, 1983.

[24] *Methodology of Integration of HVDC Links in Large AC Systems–Phase 1: Reference Manual*, EPRI EL-3004, March 1983.

[25] *Methodology of Integration of HVDC Links in Large AC Systems–Phase 2: Advanced Concepts*, EPRI EL-4365, Vol.1, April 1987.

[26] D.B. Giesner and J. Arrillaga, "Operating Modes of the 3-Phase Bridge Convertor," *International Journal of Electrical Engineering Education*, Vol. 8, 1970, pp. 373-388.

[27] *Proceedings: Bulk Power System Voltage Phenomena–Voltage Stability and Security*, EPRI EL-6183, January 1989.

[28] S.N. Chow and J. Hale, *Methods of Bifurcation Theory*, Speinger-Verlag, New York, 1982.

[29] Laszlo Gyugyi, "Power Electronics in Electric Utilities: Static Var Compensators," *Proc. of the IEEE*, Vol. 76, No. 4, April 1988, pp. 483-494.

[30] Timothy J.E. Miller, *Reactive Power Control In Electric Systems* , John Wiley & Sons, 1991.

[31] Roland Priemer, *Introductory Signal Processing*, World Scientific, 1991.

[32] "Static Var Compensators," technical report of task force 2, CIGRE, 1986.

[33] Committee on Static Compensation, *Static Compensators for reactive power control*, Canadian Electrical Association, 1984.

[34] W.L. Brogan, *Modern Control Theory*, Prentice Hall, 1991.

[35] J. Stoer and R. Bilirsch, *Introduction to Numerical Analysis*, Springer-Verlag, 1980.

[36] The Math Works Inc., Natick, Massachusetts, *MATLAB*, 1993.

[37] R.S. Ramshaw, *Power Electronics Semiconductor Switches*, Chapman & Hall, 1993.

[38] K. Clark, B. Fardanesh, R. Adapa, "Thyristor Controlled Series Compensation Application Study - Control Interaction Considerations," *IEEE Trans. on Power Delivery*, Vol. 10, No. 2, April 1995.

[39] A.R. Bergen, *Power System Analysis*, Prentice Hall, 1986.

[40] *CYMFLOW User's Guide and Reference Manual*, CYME Int., December 1987.

[41] I.S. Duff, A.M. Erisman and J.K Reid, *Direct Methods for Sparse Matrices*, Oxford Science Publications, 1986.

[42] "Extended Transient Midterm Stability Package: User's Manual for the Power Flow Program," EPRI EL-2002-CCM, January 1987.

[43] Claudio A. Canizares, Antonio C.Z. de Souza and Victor H. Quintana, " Comparison of Performance Indices for Detection of Proximity to Voltage Collapse," IEEE/PES 95SM583-5-PWRS, July 1995.

[44] IEEE Committee Report, "Common Format for Exchange of Solved Load Flow Data," *IEEE Trans. Power Apparatus and Systems*, Vol. PAS-92, No.6, Nov./Dec. 1973, pp.1916-1925.

[45] F.L. Alvarado, "Manipulation and Visualization of Sparse Matrices," ORSA Journal of Computing 2, 1990, pp. 180-207.

[46] Zeno T. Faur and Claudio A. Cañizares, "Effects of FACTS devices on system loadability," *Proc. North American Power Symposium* , Bozeman, Montana, October 1995.

[47] E. Enrique, *Sensitivity Analysis For Compensator Placement in Power Systems*, MASc Thesis, University of Waterloo, April 1994.

[48] V.H. Quintana and E.H. Enrique, "Sensitivity Analysis of Oscillation Modes in Power Systems," *Proc. North American Power Symposium*, 1994,pp. 345352.

[49] Y. Mansour, W. Xu, F. Alvarado and C. Rinzin, "SVC placement using critical modes of voltage instability," *IEEE Trans. Power Systems*, Vol.9, No.2, May 1994, pp.757-763.